

A set oriented definition of finite-time Lyapunov exponents and coherent sets

Phanindra Tallapragada ^{a,*}, Shane D. Ross ^b

^a Mechanical Engineering and Engineering Science, University of North Carolina at Charlotte, NC, USA

^b Engineering Science and Mechanics, Virginia Tech, Blacksburg, VA, USA

ARTICLE INFO

Article history:

Received 17 March 2012

Received in revised form 3 September 2012

Accepted 9 September 2012

Available online 2 October 2012

Keywords:

Phase space transport
Lagrangian coherent structures
Hyperbolic invariant manifolds
Finite time Lyapunov exponents
Almost invariant sets
Transport and mixing in fluids

ABSTRACT

The problem of phase space transport, which is of interest from both the theoretical and practical point of view, has been investigated extensively using geometric and probabilistic methods. Two important tools to study this problem that have emerged in recent years are finite-time Lyapunov exponents (FTLE) and the Perron–Frobenius operator. The FTLE measures the averaged local stretching around reference trajectories. Regions with high stretching are used to identify phase space transport barriers. One probabilistic method is to consider the spectrum of the Perron–Frobenius operator of the flow to identify almost-invariant densities. These almost-invariant densities are used to identify almost invariant sets. In this paper, a set-oriented definition of the FTLE is proposed which is applicable to phase space sets of finite size and reduces to the usual definition of FTLE in the limit of infinitesimal phase space elements. This definition offers a straightforward connection between the evolution of probability densities and finite-time stretching experienced by phase space curves. This definition also addresses some concerns with the standard computation of the FTLE. For the case of autonomous and periodic vector fields we provide a simplified method to calculate the set-oriented FTLE using the Perron–Frobenius operator. Based on the new definition of the FTLE we propose a simple definition of finite-time coherent sets applicable to vector fields of general time-dependence, which are the analogues of almost-invariant sets in autonomous and time-periodic vector fields. The coherent sets we identify will necessarily be separated from one another by ridges of high FTLE, providing a link between the framework of coherent sets and that of codimension one Lagrangian coherent structures. Our identification of coherent sets is applied to three examples.

© 2012 Elsevier B.V. All rights reserved.

1. Introduction

The problem of phase space transport has important applications in mixing and separation problems in fluid flows that vary in scale from the micro to the geophysical scale, from interplanetary transport to instability of mechanical systems, to name a few. A variety of dynamical systems methods have been studied over the past three decades to explain transport mechanisms, to detect barriers to transport, and to quantify transport rates [1–15]. These methods fall into two main categories, the geometric and the probabilistic. Under the umbrella of geometric methods are the techniques of invariant manifolds (of fixed points or larger invariant sets), lobe dynamics and finite-strain maps, finite-time Lyapunov exponents (FTLE)

* Corresponding author.

E-mail address: tsphanindra@gmail.com (P. Tallapragada).

and Lagrangian coherent structures (LCS). The method of finite-strain, FTLE and LCS has proven to be particularly useful in studying transport in time-dependent systems and has found a variety of applications [16–27]. The probabilistic approach studies the transport of densities and measures, and gives rise to notions of almost-invariant sets (AISs) and coherent sets. These methods have been successfully applied in the study of various geophysical flow problems [13] and mixing in micro-channels [28–30].

The development of the above two methods has occurred almost simultaneously in the last decade or so. The method of LCS studies stretching and contraction around reference trajectories and identifies transport barriers. The LCS method is therefore a local method; it provides local transport information from which one attempts to infer the global transport properties of the system. The probabilistic method, on the other hand, ignores the local transport structures, but using the transfer operator divides the phase space into two maximally invariant sets, i.e. ‘minimally leaky sets’.

More recently other measures to identify geometrical features and Lagrangian coherence in fluid flows have been advanced such as in [31,32]. The main idea in [32] is to use the increase in arc length of material lines as a measure of deformation of a set. In [31] the authors proposed a method to distinguish between the linearized stretching and the folding of material lines by using tools developed in the area of glassy solids. In this approach stretching (so called affine deformations) are separated from folding (so called non-affine deformations) of material lines by using the observation that stretching dominates on small time scales and folding on longer time scales. The ideas put forward in [31,32] utilize information from deformation of material lines and thus have a geometric flavor to them.

A comparison of the results of geometric and probabilistic approaches has been given in Dellnitz et al. [9] and Froyland et al. [13] for some time-independent and time-periodic vector fields in which it was shown that the LCS method does not necessarily yield optimal invariant sets. While comparison of results from different approaches in specific cases is possible the relationship between the geometric and probabilistic methods is not yet clearly understood. One of the reasons this has been difficult is that geometric methods depend on stretching of material lines (of zero Lebesgue measure) while the probabilistic method relies on identifying minimally leaky sets of positive measure. One way to address this issue is to formulate an approach that measures deformations of sets of positive measure. Such a set oriented definition of deformation of sets will be a step towards understanding the relationship between the probabilistic and geometric approaches.

In this paper we (1) propose a set-oriented definition of FTLE that offers a straightforward connection between the evolution of probability densities and finite-time stretching experienced by phase space curves, (2) propose a simplified method to calculate this quantity when the vector field is periodic using the Perron-Frobenius operator which avoids long-time integrations and (3) propose a simple definition of finite-time coherent sets for vector fields of general time dependence. We illustrate the proposed definitions with three examples, including geophysical flows defined from data.

We show that the standard FTLE of a trajectory is a special case of the set oriented FTLE of the trajectory of a local set when the measure of the set is small. We further highlight that while standard FTLE computations can identify Lagrangian coherent structures these transport barriers do not describe transport due to nonlinear stretching and folding of material lines that occur on long time scales. The set-oriented FTLE definition we put forward in this paper measures more than the local measure of stretching around trajectories and contains information on this nonlinear deformation. An important advantage of a set-oriented FTLE is that one can assign an FTLE value to a set of any size while the standard FTLE is in theory assigned to infinitesimal sets. Using this idea that one could assign an FTLE value to a large set, we propose a heuristic definition of coherent sets in flows. Here we point out that while in time-independent systems, almost-invariant sets have been defined precisely and methods to identify such sets are well established, the same is not true of time dependent systems. This is more so when one considers dynamical systems defined by data that is coarse both spatially and temporally, such as in geophysical fluid flows. Our heuristic definition of coherent sets fills this gap and can identify an approximate hierarchy of sets of specified Lebesgue measure with various degrees of coherence. This heuristic method does not necessarily optimally partition the domain into two large non-mixing sets but merely identifies subsets that remain coherent for finite times. This is especially useful for dynamical systems defined by numerical or experimental data, as we show using the example of atmospheric flow in Section 6, where it is not obvious that there should exist only two optimally non-mixing sets.

The paper is organized as follows. In Section 2 we review the theory of AISs, FTLE and LCS. In Section 3 we discuss some limitations of the methods of FTLE-LCSs and AISs when applied to time dependent systems. In Section 4 we propose a new set oriented definition of the FTLE and coherent sets and provide the details of the computations in Section 5. In Section 6 we use three examples to illustrate our definitions and methods. In the case of autonomous vector fields we also compare our results with those obtained by the classic FTLE method and the method of AIS. We do this to verify that our results on weakly mixing sets do not depart qualitatively from those obtained by the method of AIS in the case of time independent systems.

2. Review of almost-invariant sets and Lagrangian coherent structures

We review the concepts of almost invariant sets, FTLE and LCS in this section. This review is intended to provide a background and set the context for our reformulation of the FTLE and its probabilistic interpretation. For the details on these methods the reader is referred to [4–6,8,9,11,15].

2.1. Almost-invariant sets

Let μ denote the Lebesgue measure on $M \subset \mathbb{R}^n$ and $\phi(\mathbf{x})_{t_0}^t : M \times \mathbb{R} \times \mathbb{R} \rightarrow M$ be a flow map on M from time t_0 to t . Let B be a measurable set and $f \in L^1$ be a probability density function, L^1 being the space of Lebesgue integrable functions. The unique operator $\mathcal{P}_{t_0}^t : L^1 \mapsto L^1$ defined by

$$\int_B \mathcal{P}_{t_0}^t f d\mu = \int_{(\phi_{t_0}^t)^{-1}(B)} f d\mu \tag{1}$$

is called the Perron–Frobenius operator for the flow map $\phi_{t_0}^t$, [33]. Eq. (1), which holds for all measurable sets, follows from the Radon–Nykodym theorem.

In practice it is usually necessary to numerically approximate the operator $\mathcal{P}_{t_0}^t$. This is done by discretizing the domain, M , into a finite number of sets, say $\{B_1, B_2, \dots, B_n\}$ which is essentially a grid of boxes. A projection $\pi : L^1 \mapsto \text{span}\{\mathcal{X}_{B_1}, \dots, \mathcal{X}_{B_n}\}$ defined by $\pi f = \sum_{i=1}^n c_i \mathcal{X}_{B_i}$, where \mathcal{X}_{B_i} is the characteristic function of the set B_i and $c_i = \frac{\int_{B_i} f d\mu}{\mu(B_i)}$ gives a finite dimensional approximation of f . Since f is a probability density function, $c_i = \frac{1}{\mu(B_i)}$. Similarly, $\mathcal{P}_{t_0}^t f$ is projected on $\text{span}\{\mathcal{X}_{B_1}, \dots, \mathcal{X}_{B_n}\}$. The operator $P_{t_0}^t : \pi f \mapsto \pi \mathcal{P}_{t_0}^t f$ is a linear operator between finite dimensional vector spaces. Further taking the box measures $\mu(B_i) = \mu(B_j)$ for all $i, j \in \{1, \dots, n\}$, $P_{t_0}^t$ becomes a stochastic transition matrix. The entries of the matrix P can be determined by a Monte-Carlo simulation [8]. Each box in the domain contains a fixed number of points (initial conditions) which are integrated from a time t_0 to t . The final position of the points gives the matrix P as,

$$(P_{t_0}^t)_{ij} = \frac{\mu(B_i \cap (\phi_{t_0}^t)^{-1}(B_j))}{\mu(B_j)}. \tag{2}$$

A time-reversible operator P_r , is useful at this point [34], defined as,

$$(P_{t_0}^t)_r = \frac{(P_{t_0}^t) + \overline{(P_{t_0}^t)}}{2} \tag{3}$$

where \overline{P} is the time reversed analogue of P . Its elements are given by

$$\overline{(P_{t_0}^t)}_{ij} = \frac{w_{1j} (P_{t_0}^t)_{ji}}{w_{1i}} \tag{4}$$

where w_{1k} is the k th component of the first left eigenvector, w_1 , of $P_{t_0}^t$. For a volume preserving flow map in which the domain is uniformly discretized, in our case into equal sized boxes, $\overline{P_{t_0}^t} = (P_{t_0}^t)^*$, the transpose of $P_{t_0}^t$. The Markov operator P has the semigroup property of $P_{t_0}^t = P_s^s P_{t_0}^t$, where $s \in (t_0, t)$. In Section 5 this property is used to simplify the computations of the FTLE for periodic systems.

A probability density function f is invariant under the flow map if and only if f is a fixed point of P , i.e., $f = Pf$ [33]. The Radon–Nikodym theorem guarantees the existence of a measure $\mu_f = \int f d\mu$ that is absolutely continuous with respect to μ . The measure μ_f associated with the invariant density is called the invariant measure of the flow map [15]. We make the additional observation that from (1), it follows that if $f > 0$, then $Pf > 0$ almost everywhere. A set $B \in \mathcal{B}$ is considered almost-invariant over the interval $[t_0, t]$ if,

$$\rho_{\mu_f}(B; t_0, t) = \frac{\mu_f(B \cap (\phi_{t_0}^t)^{-1}(B))}{\mu_f(B)} \approx 1. \tag{5}$$

In practice one seeks to maximize the following discretized version of ρ_{μ_f} over all possible sets $B = \cup_i B_i$,

$$\rho_{\mu_f}(B) = \frac{\sum_{i,j} w_{1j} (P_{t_0}^t)_{ji}}{\sum_j w_{1j}}. \tag{6}$$

One can in theory construct an optimization problem to maximize the value of ρ_{μ_f} over all possible combinations of sets $B \in \mathcal{B}$. But this problem is combinatorially hard to solve even for simple flow maps. Therefore heuristic methods advanced in [8,11] are adopted to identify maximally AISs.

It was shown in [8,35,11] that the second right eigenvector, v^2 of P_r corresponding to λ_2 , the second eigenvalue, optimizes value of ρ_{μ_f} , the invariance being higher if λ_2 is closer to 1. The domain is divided into two almost invariant sets, B^+ and B^- according to the rule

$$B^+ = \bigcup_{i: v_i^2 > 0} B_i \quad \text{and} \quad B^- = \bigcup_{i: v_i^2 < 0} B_i. \tag{7}$$

The matrix P_r is self-adjoint and so the left and right eigenvectors u and v form an orthonormal basis. The first eigenvector v^1 , associated with the eigenvalue 1, is the stationary distribution and is positive. Since $v^2 \perp v^1$ we can infer that v^2 has both

positive and negative parts. From the definition of a Markov operator, $P_r(v^2)^+ > 0$ and $P_r(v^2)^- < 0$, where $(v^2)^+$ and $(v^2)^-$ are the positive and negative parts of v^2 such that $v^2 = (v^2)^+ + (v^2)^-$. So the sets on which the positive and negative parts of the second eigenvector v^2 are supported are AIs and partition the domain M into two parts of equal measure. It should be noted that since P_r is self-adjoint in our examples of volume preserving flows in Sections 6.1 and 6.2, the matrix of left eigenvectors U is the adjoint of the matrix of the right eigenvectors V . Hence the heuristic analogous to (7) could be used with the right eigenvector, v^2 , instead of the left eigenvector, u_2 .

2.2. FTLE and LCS

Let the differential equations corresponding to the flow map defined by $\phi(\mathbf{x})_{t_0}^t : M \times \mathbb{R} \times \mathbb{R} \rightarrow M$ be the equations $\dot{\mathbf{x}} = \mathbf{F}(\mathbf{x}, t)$. Thus the linearized variational equation is

$$\delta\dot{\mathbf{x}}(t) = \frac{D\mathbf{F}}{D\mathbf{x}} \delta\mathbf{x}(t), \tag{8}$$

where $\delta\mathbf{x}(t)$ is a perturbation or more accurately an element in $T_{\mathbf{x}}M$, the tangent space of M at $\mathbf{x}(t)$ and $\frac{D\mathbf{F}}{D\mathbf{x}}$ is evaluated along the trajectory.

Definition 2.1. The maximum Lyapunov exponent is defined as, [36]

$$\sigma(\mathbf{x}) = \limsup_{t \rightarrow \infty} \frac{1}{t} \log \frac{\|\delta\mathbf{x}(t)\|}{\|\delta\mathbf{x}(t_0)\|}. \tag{9}$$

Thus, the Lyapunov exponent measures the maximum time averaged stretching of line elements in a small neighborhood along a trajectory. Since many time-dependent systems of interest are either defined for only finite times (such as by numerical or experimental data) and also possess interesting phase space structures on finite time scales, a finite time version of the Lyapunov exponent that is based on the finite time stretching of line elements is often employed to study phase space transport.

Consider a reference trajectory passing through the point $\mathbf{x}(t_0)$ and a perturbed trajectory passing through the point $\mathbf{x}(t_0) + \delta\mathbf{x}(t_0)$ at time t_0 . The flow map $\phi_{t_0}^t$ maps these points to $\phi_{t_0}^t(\mathbf{x}(t_0))$ and $\phi_{t_0}^t(\mathbf{x}(t_0) + \delta\mathbf{x}(t_0))$ at time t and the perturbation grows to $\delta\mathbf{x}(t)$. Expanding $\phi_{t_0}^t(\mathbf{x}(t_0) + \delta\mathbf{x}(t_0))$ in a Taylor series about the point $\mathbf{x}(t_0)$ we get,

$$\delta\mathbf{x}(t) = \phi_{t_0}^t(\mathbf{x}(t_0) + \delta\mathbf{x}(t_0)) - \phi_{t_0}^t(\mathbf{x}(t_0)) = \frac{d\phi_{t_0}^t}{d\mathbf{x}} \delta\mathbf{x}(t_0) + O(\|\delta\mathbf{x}(t_0)\|^2). \tag{10}$$

The norm or magnitude of $\delta\mathbf{x}(t)$ can be found using the standard inner product on \mathbb{R}^n .

$$\|\delta\mathbf{x}(t)\| = \sqrt{\left\langle \frac{d\phi_{t_0}^t}{d\mathbf{x}} \delta\mathbf{x}(t_0), \frac{d\phi_{t_0}^t}{d\mathbf{x}} \delta\mathbf{x}(t_0) \right\rangle} = \sqrt{\left\langle \delta\mathbf{x}(t_0), \left(\frac{d\phi_{t_0}^t}{d\mathbf{x}} \right)^* \frac{d\phi_{t_0}^t}{d\mathbf{x}} \delta\mathbf{x}(t_0) \right\rangle}, \tag{11}$$

where $*$ denotes the transpose and the gradient $\left(\frac{d\phi_{t_0}^t}{d\mathbf{x}} \right)$ is evaluated at $\mathbf{x}(t_0)$. The maximum growth of a perturbation is therefore given by the maximum principal stretch, i.e., by the maximum eigenvalue of C .

$$\max \|\delta\mathbf{x}(t)\| = \sqrt{\lambda_{\max}(C(\mathbf{x}(t_0), t_0, t))} \|\delta\mathbf{x}(t_0)\|, \tag{12}$$

where $C(\mathbf{x}(t_0), t_0, t) = \left(\frac{d\phi_{t_0}^t}{d\mathbf{x}} \right)^* \left(\frac{d\phi_{t_0}^t}{d\mathbf{x}} \right)$ is the Cauchy–Green tensor. The growth in the perturbation depends on the initial point \mathbf{x} , initial time t_0 and the evolution or integration time $T = t - t_0$.

Definition 2.2. The maximum FTLE is defined as, [4,5],

$$\sigma(\mathbf{x}(t_0), t_0, t) = \frac{1}{|t - t_0|} \log \left(\sqrt{\lambda_{\max}(C(\mathbf{x}(t_0), t_0, t))} \right). \tag{13}$$

The leading FTLE gives the time averaged rate of linearized stretching in a neighborhood around a reference trajectory. It is intuitively clear that regions of the phase space with locally high values of FTLE will undergo high stretching. The sets with high FTLE act as repelling barriers in the flow map. This intuitive idea of barriers is formalized by the concept of Lagrangian coherent structures (LCS) due to Haller and Yuan [37,38] and Lekien, Shadden and Marsden [4,5].

Definition 2.3. LCS are codimension one ridges in the scalar FTLE field $\sigma(\mathbf{x}, t_0, t)$.

Ridges can be defined precisely by appealing to differential geometric quantities [39,4,5,40]. Another alternative definition of LCS, due to Haller [7], defines LCS more restrictively as hyperbolic material surfaces that extremize finite time normal repulsion or attraction. This eliminates spurious LCS such as those due to shear stretching.

3. Limitations of the methods of FTLE-LCSs and AISs in time-dependent vector fields

Limitations of LCS. The concepts of FTLE and LCS reviewed previously have been used fruitfully in many areas as has been pointed out earlier. However the standard computational implementation of FTLE, using finite differences, [22,4], suffers from some drawbacks, stemming from the integration time T and the linearization around reference trajectories. In (10), it is assumed that the second (and higher) order terms are negligible. However the magnitude of the higher order terms depends on the evolution time $T = t - t_0$. If the evolution time T is too high then the higher order terms may be comparable to the first order terms in (10). If the evolution time T is too low, then one cannot detect any interesting structure in the FTLE field. While there is some interesting work on choosing T for finite dispersion calculations in [41], often T is selected in a subjective fashion without checking the validity of (10). In a long integration period, the FTLE may underestimate the deformation of some material lines. We illustrate the problem with long time integration with the example of the double gyre flow, a prototype in the LCS literature, [4,42]. The double gyre velocity field is defined by the stream function $\psi(x, y, t) = A \sin(\pi f(x, t)) \sin(\pi y)$, with $f(x, t) = \epsilon x^2 \sin \omega t + x(1 - 2\epsilon \sin \omega t)$, where we use the parameters $A = 0.25$, $\omega = 2\pi$ and $\epsilon = 0.25$. The time period of the vector field is $\tau = 1$. The FTLE field for the double gyre flow for these parameters is shown in Fig. 2.

Now consider (10) with the second-order terms explicitly written,

$$\delta \mathbf{x}(t_0 + t) = \phi_{t_0}^t(\mathbf{x}) - \phi_{t_0}^t(\mathbf{x} + \delta \mathbf{x}) = \frac{d\phi_{t_0}^t}{d\mathbf{x}} \delta \mathbf{x}(t_0) + \frac{1}{2} \delta \mathbf{x}(t_0)^* \frac{d^2 \phi_{t_0}^t}{d\mathbf{x}^2} \delta \mathbf{x}(t_0) + O(\|\delta \mathbf{x}(t_0)\|^3). \tag{14}$$

In this equation it can be shown that the second and first order terms are comparable in magnitude. The max-norm for matrices is used for this comparison. Fig. 3 shows the plot of $\lambda_{\max} \left(\frac{d\phi_{t_0}^t}{d\mathbf{x}} \right) \|\delta \mathbf{x}\|$ and $\frac{1}{2} \lambda_{\max} \left(\frac{d^2 \phi_{t_0}^t}{d\mathbf{x}^2} \right) \|\delta \mathbf{x}\|^2$. In the region around the ridges, the magnitude of the second-order terms is more than half that of the first-order terms in (14). This is true for a smaller evolution time as well, such as $T = 5$. For smaller integration time such as $T = 1$ the ridges are not prominent enough. The ridges in the FTLE field for the double gyre are generated by moving instantaneous stagnation points (ISPs). Material line elements close to the ISPs stretch in a shorter time as compared to material line elements farther away. Therefore

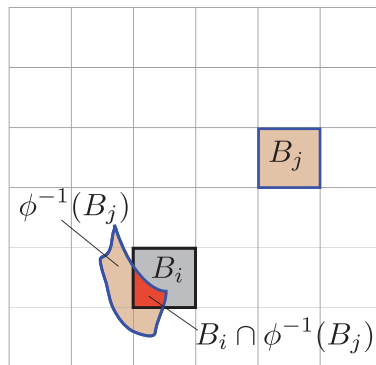


Fig. 1. Box-discretization method to calculate P . Box B_j at the final time t is mapped (backwards) to $\phi^{-1}(B_j)$ at the initial time t_0 . The value of the entry P_{ij} is the fraction of box B_i that is mapped into box B_j by ϕ . Note that $\sum_{j=1}^n P_{ij} = 1$.

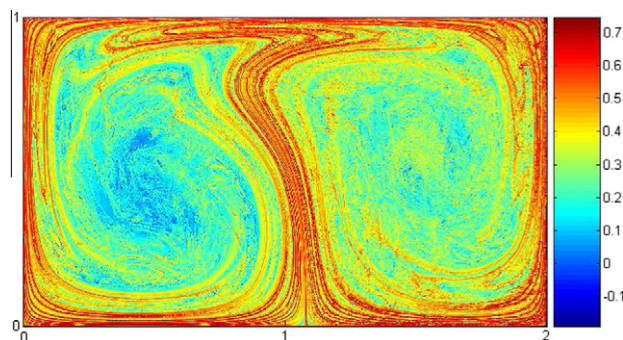


Fig. 2. FTLE field for the double gyre system for $T = t - t_0 = 10$.

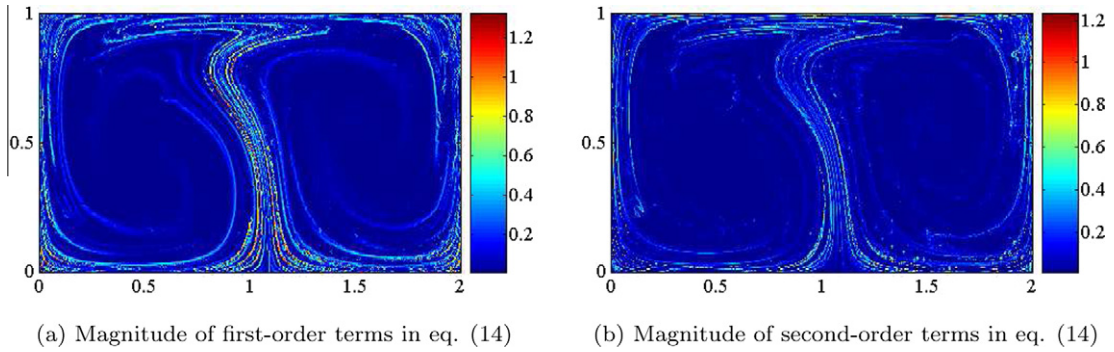


Fig. 3. (a) Comparison of first- and second-order terms in Eq. (14) for $T = t - t_0 = 10$.

identifying interesting structures such as ridges in the FTLE field requires a long period of integration during which the non-linear deformation of line elements close to the ISPs occurs.

The problem of the high magnitude of second order terms is not merely due to the coarseness of the grid. It can be seen that stretching of material lines in the double gyre is due to moving instantaneous saddle points on the lines $y = 0$ and $y = 1$. So even if one were to take a finer grid of initial conditions, once two points begin to separate exponentially around the saddle point the material line joining them also stretches to a length that cannot be accounted by the linear approximation. Thus the linearized approximation can be erroneous for any discretization of initial conditions.

An alternative, albeit older, method to calculate Lyapunov exponents exists, which has not been widely used to identify Lagrangian coherent structures. The details of this method can be found in the paper by Swinney et al. [43] and have been applied for geophysical flows in [16,17]. In this method, the linearized variational equations, (8), are used to calculate the time rate of expansion of vectors in the tangent space, $(\delta \mathbf{x} \in T_x M)$. As the tangent vectors grow in magnitude, they are renormalized and the integration of the linearized equations is continued. The averaged rate of expansion of the tangent vectors over the time of integration gives the Lyapunov exponent. In principle this method is the same as the previous one. This is because $\frac{d\mathbf{F}}{d\mathbf{x}} = \left(\frac{d}{dx} \frac{d\phi}{dt}\right) = \left(\frac{d}{dt} \frac{d\phi}{dx}\right)$, assuming equality of mixed partial derivatives of the flow map ϕ . Thus the time averaged logarithm of the maximum norm of the tangent map $\frac{d}{dx}$ gives the maximum Lyapunov exponent. The variational equations can be integrated with a high degree of accuracy for analytically defined dynamical systems. But in the case of equation free systems defined by numerical data, the calculation of the Jacobian using coarse data leads to the same problem of large second order terms. Moreover, when calculating the Jacobian from numerical data it is also possible to underestimate the FTLE. This is because when material lines fold excessively as shown in Fig. 4, finite differencing underestimates the terms in the Jacobian.

While the errors in accurately calculating the FTLE can be rectified at least for systems where the variational equations can be calculated as accurately as desired, there emerges another subtle point from the example of the double gyre. When one is interested in the finite time global transport and transport barriers, nonlinear stretching and folding of material lines play an important role, see for example [31]. Even an accurately calculated FTLE does not quantify this simply because the Lyapunov exponents are defined for the linearized variational equations. This is an inherent feature to the double gyre as well as other time dependent systems and is not due to the particular computational method or coarsely discretized initial

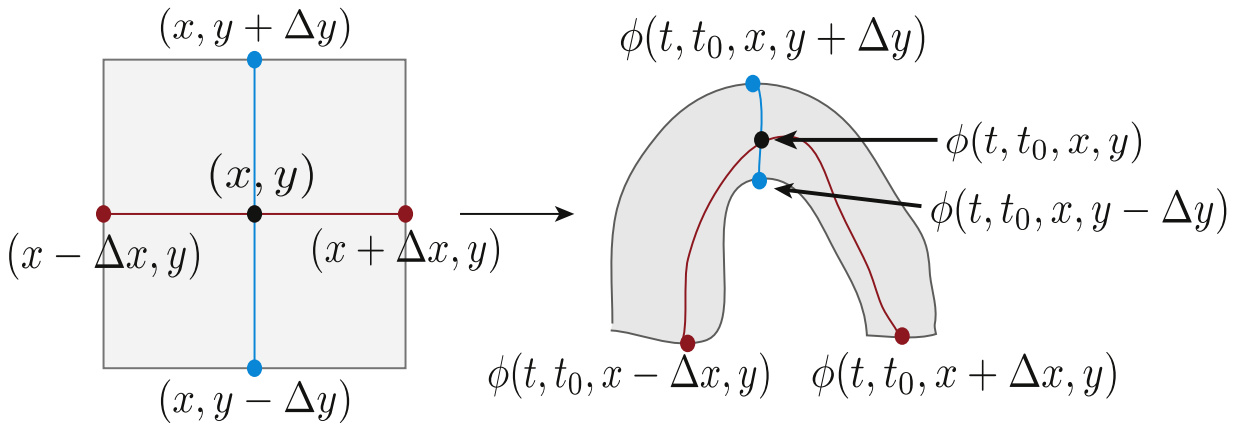


Fig. 4. Even though the material line joining $(x - \Delta x, y)$ and $(x + \Delta x, y)$ has stretched considerably under the flow map, the ratio $\frac{\phi_{t_0}^t(x + \Delta x, y) - \phi_{t_0}^t(x - \Delta x, y)}{2\Delta x}$ is less than 1.

conditions. Put simply, the FTLE/LCS method does not address the importance of transport on finite time-scales due to the higher order terms in (10). Our aim in the subsequent sections is to define an FTLE-like quantity that is based on the deformations of sets instead of the linearized stretching of line elements. Such a quantity will measure the nonlinear deformation of a set.

Another limitation of the method of LCS is that it often identifies too much structure in the flow map. In complex flows like the atmosphere almost every trajectory can have high localized expansion around it. The resulting FTLE field has a network of sharp ridges with small length scale that exist for short periods of time. Such structures may not be of interest in the study of large scale transport. There is no systematic method of obtaining large scale transport barriers from the small scale structures. A set-oriented definition of the FTLE can identify the deformation of any connected set. As we show in Section 6 our set oriented definition of the FTLE enables the computation of the FTLE for large sets.

Limitations of AISs. The division of the phase space into two AISs using the Perron–Frobenius operator, P , has a physical meaning in terms of mixing; the two AISs identified by the positive and negative portions of the second eigenvector of P do not mix significantly with each other. But this method of identifying AISs does not discriminate between deformation of sets and translation of sets in time-dependent systems. The problem is illustrated in Fig. 5. Sets B_1 and B_2 , advected by the flow map $\phi_{t_0}^t$, do not distort and mix with each other or the rest of the domain. However, there is no ‘overlap’ between the regions $\{B_1, B_2\}$ and their images $\{\phi_{t_0}^t(B_1), \phi_{t_0}^t(B_2)\}$, because the flow map ‘translates’ them. Sets B_1 and B_2 are definitely not invariant or almost-invariant since they do not overlap with $\phi_{t_0}^t(B_1)$ or $\phi_{t_0}^t(B_2)$, respectively. The sets B_1 and B_2 cannot be identified as almost invariant by the second eigenvalue–eigenvector of P . Sets B_3 and B_4 clearly have distorted and mixed partially with each other and the rest of the domain. The second eigenvector of P does not differentiate between the two cases, even though B_1 and B_2 can be intuitively understood to be coherent, while B_3 and B_4 are not.

It becomes even more difficult to apply the definition of AISs to vector fields defined by numerical or experimental data in which the domain is ‘leaky’. Particles that exit the domain of the data are either lost or have to be tracked using a combination of interpolations or very coarse data. For a leaky domain the first eigenvalue of P is not 1 and the criterion of the second eigenvalue being close to 1 can become problematic. Lastly, the method of AIS does not directly deal with the mechanisms of transport, such as the stable and unstable manifolds of fixed points and the ridges in the FTLE field and the associated lobe dynamics.

One possible extension of the concept of AISs to coherent sets in time-dependent systems has been done [12,13]. A set B was defined to be coherent if it almost mapped to $\phi_{t_0}^t(B)$ under a small noise. The phase space is divided into two optimally coherent sets in a heuristic manner out of all the possible combinations of the subsets. However the method given in [13], partitions the domain into two large coherent sets of similar size. It was noted in [13] that from those sets that stretch and become very thin, particles can be ejected easily with a small amount of diffusion. We make explicit use of this idea in our definition of coherent sets. We provide a method which can identify multiple disconnected coherent sets in a domain. We do this by first providing an alternative set oriented definition of the FTLE.

4. Set-oriented definition for FTLE and coherent sets

We formulate a new definition of the FTLE that does not use the linearized equations of the flow map, or the stretching of individual line elements. To illustrate the concept we assume the flow map is over \mathbb{R}^2 with $(x_1, x_2) \in \mathbb{R}^2$. The method of

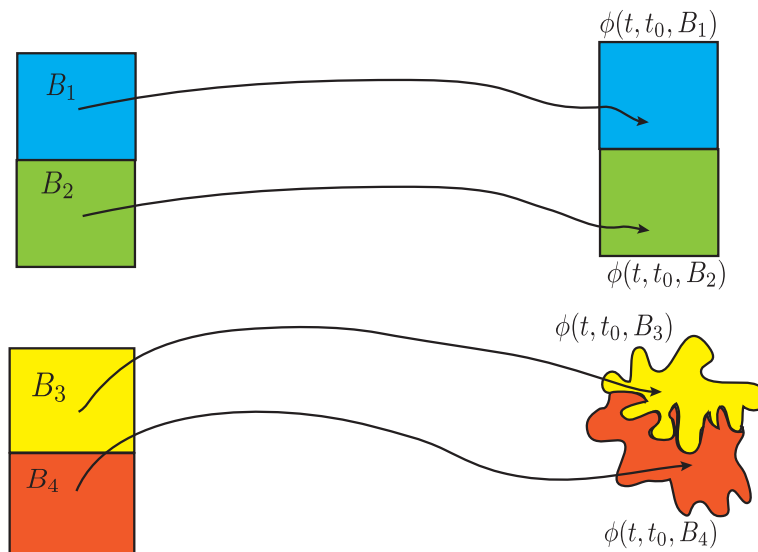


Fig. 5. None of the sets B_1, B_2, B_3 or B_4 are almost-invariant.

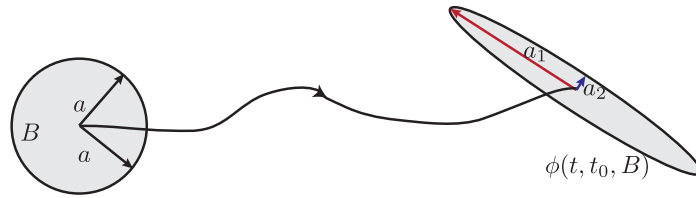


Fig. 6. Deformation of a disk under the flow map.

computing FTLE using the eigenvalue decomposition (SVD) of the Cauchy–Green tensor essentially computes the deformation of a neighborhood under the action of the flow map $\phi_{t_0}^t$ as shown in Fig. 6. The FTLE for the reference trajectory in this case is $\sigma = \frac{1}{|T|} \log \left(\frac{a_1}{a} \right)$ where $T = t - t_0$ is the evolution time of the trajectory. This is a measure of the deformation of a circle of radius a into an ellipse with major and minor axes a_1 and a_2 , respectively.

The set B is tracked by the evolution of a vector $X = [X_1, X_2]$ defined by a probability density function $f(x_1, x_2)$ which is initially a uniform probability density function supported on B given by, $f = \frac{1}{\mu(B)} \mathcal{X}_B$, where \mathcal{X}_B is the characteristic function of B . The covariance matrix of f is $I_{ij} = E[(X_i - \bar{X}_i)(X_j - \bar{X}_j)]$, with $i, j = 1, 2$ where $[\bar{X}_1, \bar{X}_2]$ is the mean value of the random vector X and $E[\cdot]$ denotes the expectation with $E[X] = [\int x_1 f(x_1, x_2) d\mu, \int x_2 f(x_1, x_2) d\mu]$. Under the action of the flow map $\phi_{t_0}^t, f$ is mapped to $\mathcal{P}_{t_0}^t f$ where $\mathcal{P}_{t_0}^t$ is the associated Perron–Frobenius operator.

Definition 4.1. Let $I(f)$ be the covariance of f and $I(\mathcal{P}f)$ the covariance of $\mathcal{P}f$ and let $\lambda_{\max}(I)$ denote the maximum eigenvalue of I . Then the FTLE of B denoted by $\sigma_I(B, t_0, t)$ is defined as,

$$\sigma_I(B, t_0, t) = \frac{1}{|t - t_0|} \log \left(\frac{\sqrt{\lambda_{\max}(I(\mathcal{P}f))}}{\sqrt{\lambda_{\max}(I(f))}} \right). \tag{15}$$

It can be shown by direct calculation that the covariance FTLE obtained from this definition and the standard FTLE (Definition 2.2) have the same value if the second and higher order terms in (14) are negligible when compared to the first order terms. In this case an initial circular blob deforms into an ellipse as shown in Fig. 6. The eigenvalues of the Cauchy–Green tensor, C , are a_1^2 and a_2^2 . The standard FTLE is $\sigma = \frac{1}{|t-t_0|} \log \frac{a_1}{a}$. The covariance matrix $I(\mathcal{P}f)$ is a diagonal matrix with $I(\mathcal{P}f)_{11} = \frac{1}{4} \pi a_1^3 a_2$ and $I(\mathcal{P}f)_{22} = \frac{1}{4} \pi a_1 a_2^3$ giving $\lambda_{\max}(I(\mathcal{P}f)) = \frac{1}{4} \pi a_1^3 a_2$. The covariance matrix $I(f)$ is a diagonal matrix with $I(f)_{11} = I(f)_{22} = \frac{1}{4} \pi a^4$ giving $\lambda_{\max}(I(f)) = \frac{1}{4} \pi a^4$. This gives the covariance FTLE, $\sigma_I = \frac{1}{|t-t_0|} \log \left(\frac{\sqrt{\frac{a_1^3 a_2}{a^4}}}{\sqrt{a^4}} \right)$. For volume preserving flow maps, $\pi a_1 a_2 = \pi a^2$. This gives the covariance FTLE, $\sigma = \frac{1}{|t-t_0|} \log \frac{a_1}{a}$, the same value as the standard FTLE if the higher order terms in (10) are negligible.

The definition of σ_I avoids the linearization of the flow map and the computation of the stretching of line elements. Further it is a set-oriented method and directly computes the finite time deformation of a set. The σ_I of any arbitrary large set is well defined and can be calculated easily. Since I is the covariance matrix of f , it provides a probabilistic interpretation of the FTLE. Simultaneously I can also be interpreted as the moment of inertia of the set B and provides a geometric description of the deformation or distortion of the set. Thus the covariance based FTLE provides both a geometric and probabilistic description of the deformation of a set.

As described in Section 3, deformation of sets provides the motivation to define coherent sets. Loosely speaking, from (5), a set B_i is almost-invariant under the flow map $\phi_{t_0}^t$ if $P\mathcal{X}_{B_i} \approx \mathcal{X}_{B_i}$. The difference between $P\mathcal{X}_{B_i}$ and \mathcal{X}_{B_i} has been measured by the second eigenvalue and eigenvector of P , [8]. For the case of non-autonomous systems where coherent sets can translate and rotate, one way to view this difference is in terms of stretching measured by second moments of the probability density functions. In Fig. 7, the set B_1 is not stretched significantly and remains almost invariant while the set B_2 is stretched and is 'less' invariant. The inequality of \mathcal{X}_{B_i} and $P\mathcal{X}_{B_i}$ is captured by the second moments, that is, the covariance matrices of \mathcal{X}_{B_i} and $P\mathcal{X}_{B_i}$. It is not possible to directly quantify the transport from one set to another from the FTLE, except in the case of linear vector fields. The qualitative relationship between stretching defined by the covariance matrix and almost-invariance can be used to define the analogues of AIS in time-dependent systems, as follows,

Definition 4.2. The coherence of a set B during $[t_0, t]$ is $\sigma_I(B, t_0, t)$.

Definition 4.3. A set B is almost-coherent during $[t_0, t]$ if $\sigma_I(B, t_0, t) \approx 0$.

This definition of coherence captures the essential feature of a coherent set: it does not mix or spread significantly in the domain. To further illustrate the relation between coherence as defined here and mixing, consider the two sets B_1 and B_2 shown in Fig. 8. Also suppose sets B_1 and B_2 (of equal Lebesgue measure) contained a homogeneous distribution of two different types of tracers initially. After the finite time $t - t_0$ the largest ball in B_1 that contains only tracer 1 almost everywhere within is B_R with $\mu(B_R(x) \cap \phi(B_1)) = \mu(B_R(x))$ for some $x \in \phi(B_1)$. The largest ball in B_2 that contains only tracer 2 almost

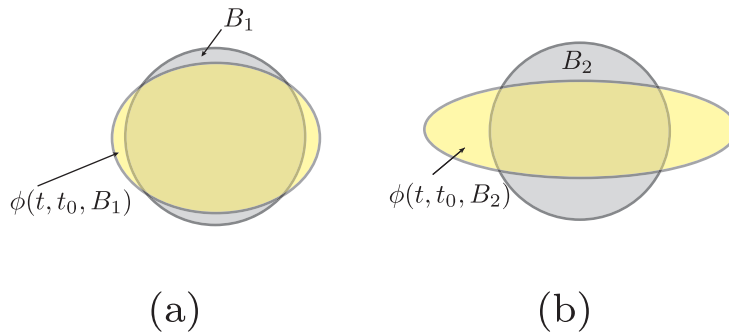


Fig. 7. Stretching and almost invariant sets: (a) set B_1 is almost invariant while (b) set B_2 is not.

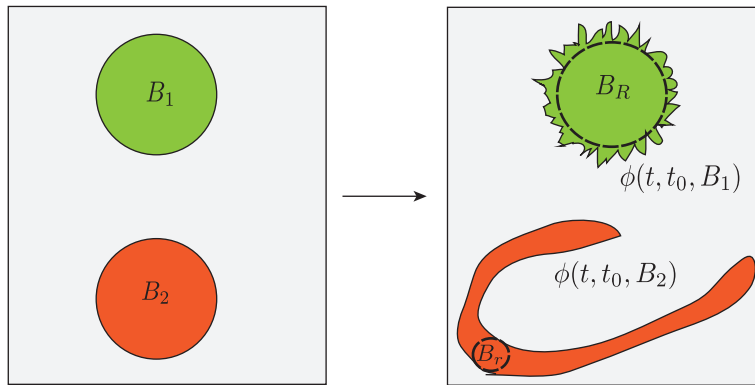


Fig. 8. The sets B_1 and B_2 are mapped to $\phi(B_1)$ and $\phi(B_2)$, respectively during which the boundaries of the sets have increased in length by at least a factor of 2. Material lines in interior of these sets could have stretched too. Yet set $\phi(B_1)$ is a coherent set since its covariance is almost the same as that of B_1 while the set $\phi(B_2)$ does not remain coherent since the covariance of $\phi(B_2)$ is much greater than that of B_2 .

everywhere within is $B_r(x)$ with $\mu(B_r(x) \cap \phi(B_2)) = \mu(B_r(x))$ for some $x \in \phi(B_2)$. The size of B_R is larger than B_r , i.e. $\mu(B_R) > \mu(B_r)$. Thus coherent sets are those that have not mixed well with the rest of the domain. This definition can also identify non-mixing translating sets of the type shown schematically in Fig. 5. In particular, values of $\sigma_l(x, t_0, t)$ determine the family of sets of various degrees of coherence. Coherent sets can be identified by setting a heuristic threshold, say σ_l^{\max} , and considering as coherent sets the regions where $\sigma_l \leq \sigma_l^{\max}$. Thus, viewing $\sigma_l(x)$ as a graph over the domain M , the coherent sets are the ‘valleys’ of the graph, which will naturally be separated from one another by the ridges of the graph, which may coincide with the LCSs.

Note that the sets identified in this way remain coherent only for times within the interval $[t_0, t]$. From our numerical computations on smooth flow maps, coherent sets vary smoothly with t , i.e., those identified by $\sigma_l(B, t_0, t_1)$ and $\sigma_l(B, t_0, t_2)$ are qualitatively similar if $|t_1 - t_2|$ is small.

4.1. Advantages of the proposed definitions of FTLE and coherent sets

1. The theory of the classic FTLE is based on linearized stretching around individual trajectories. In practice the classic FTLE method calculates the field $\sigma(x, t_0, t)$ at specified grid points. This is a measure of time averaged linearized stretching at the grid points only, from which there is no way to say how much a large set of positive measure deforms in a finite time. On the other hand, the set-based FTLE $\sigma_l(B, t_0, t)$ assigns an FTLE value to sets of positive measure. Knowing the value of $\sigma_l(B_i, t_0, t)$ one can calculate the FTLE value for $B = \cup_i^n B_i$. The set-based FTLE connects the local deformation around a trajectory to the statistics of a cluster of trajectories. In practice the set-based FTLE computations can rely on long time integrations that produce nonlinear stretching and folding.
2. The definition of the set oriented FTLE and coherence of a set is a direct measure of the dispersion of a set. A set could remain coherent even if its boundary or material lines within its interior stretch and fold. In the worst case the boundary of the set could stretch many times over and attain a fractal like structure as shown in Fig. 8, but need not spread out. The value of $\sigma_l(B, t_0, t)$ remains small for such sets.
3. The set oriented FTLE does not rely on the assumption of hyperbolicity of the flow map. However as we showed with the example of the deformation of the ellipse, if such exponentially expanding and contracting directions exist then the set oriented FTLE and the classic FTLE have the same value for a small time of integration. Thus the standard FTLE is a special case of the set oriented FTLE.

- The set oriented FTLE method assigns a coherence value to every box B_i and any set which is composed of such boxes in the domain. Even though the identification of large coherent sets relies on a heuristic threshold, this has the advantage of identifying sets of various degrees of coherence and size in the domain.

5. Computation of σ_t

For computational purposes we divide the domain into n equal boxes B_1, B_2, \dots, B_n each with a fixed number of initial points (say N) (see Fig. 1). The points in a box B have coordinates $(x_{1i}, x_{2i}), i$ ranging from 1 to N . Each of these N points has discrete measure 1. Note that each of the sets B_i has discrete measure N , a scaled approximation of the Lebesgue measure or area of the boxes. The initial probability density function initially supported on the set B is $f = \frac{1}{\mu(B)} = \frac{1}{N}$. Let the mean of each box be initially denoted by (\bar{x}_1, \bar{x}_2) , where

$$(\bar{x}_1, \bar{x}_2) = \sum_i^N ((x_{1i}, x_{2i})f) = \frac{1}{N} \left(\sum_i^N x_{1i}, \sum_i^N x_{2i} \right). \tag{16}$$

Then the covariance of the initial probability density function, $I(f)$, is given by

$$I(f) = \frac{1}{N} \begin{bmatrix} \sum_{i=1}^N (x_{1i} - \bar{x}_1)^2 & \sum_{i=1}^N (x_{1i} - \bar{x}_1)(x_{2i} - \bar{x}_2) \\ \sum_{i=1}^N (x_{1i} - \bar{x}_1)(x_{2i} - \bar{x}_2) & \sum_{i=1}^N (x_{2i} - \bar{x}_2)^2 \end{bmatrix}. \tag{17}$$

The set $\phi_{t_0}^t(B)$ is approximated by the collection of the points $\phi_{t_0}^t(x_{1i}, x_{2i})$, where $i = 1, 2, \dots, N$. Since the image probability density function, $I(Pf)$, is supported on $\phi_{t_0}^t(B)$, the numerical calculation of the covariance, $I(Pf)$, is

$$I(Pf) = \frac{1}{N} \begin{bmatrix} \sum_{i=1}^N (\phi_{t_0}^t(x_{1i}) - \bar{\xi}_1)^2 & \sum_{i=1}^N (\phi_{t_0}^t(x_{1i}) - \bar{\xi}_1)(\phi_{t_0}^t(x_{2i}) - \bar{\xi}_2) \\ \sum_{i=1}^N (\phi_{t_0}^t(x_{1i}) - \bar{\xi}_1)(\phi_{t_0}^t(x_{2i}) - \bar{\xi}_2) & \sum_{i=1}^N (\phi_{t_0}^t(x_{2i}) - \bar{\xi}_2)^2 \end{bmatrix}, \tag{18}$$

where

$$(\bar{\xi}_1, \bar{\xi}_2) = \frac{1}{N} \left(\sum_i^N \phi_{t_0}^t(x_{1i}), \sum_i^N \phi_{t_0}^t(x_{2i}) \right) \tag{19}$$

is the mean or expected value of the discrete approximation of $\phi_{t_0}^t(B)$. These calculations are illustrated in Fig. 9. The N points in box B are mapped to their images by the flow map. The initial mean (\bar{x}_1, \bar{x}_2) is calculated using (16). Similarly the mean of the image set, $(\bar{\xi}_1, \bar{\xi}_2)$, is calculated using (19). In both cases the mean is merely the geometric centroid of the set. Further we note that $(\bar{\xi}_1, \bar{\xi}_2) \neq \phi_{t_0}^t(\bar{x}_1, \bar{x}_2)$, the image of the mean need not be the mean of the image set. The covariance of the set B and $\phi_{t_0}^t(B)$ are calculated from the relative positions of the N points around the respective means using formulae (17) and (18).

The maximum eigenvalues of $I(f)$ and $I(Pf)$ are used in (15) to give the covariance FTLE. The covariance of a set A formed by combining box sets, $A = \cup_k B_k$, is found about the mean of A . Geometrically, (18) measures the covariance or the moment of inertia of a cloud of N points distributed in a planar domain.

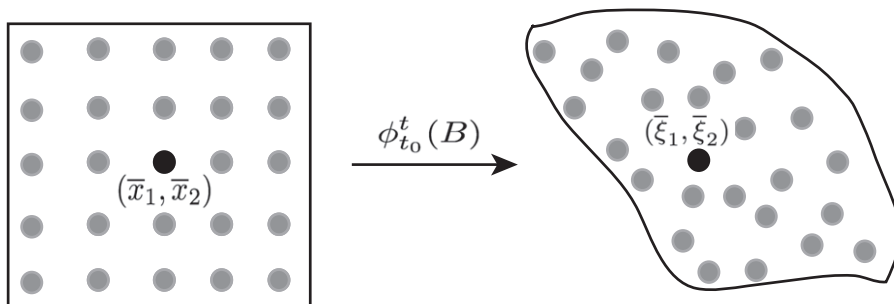


Fig. 9. Illustration of the numerical calculation of the mean and covariance, in (16)–(18). The set B approximated by the N points is mapped to the set $\phi_{t_0}^t(B)$. The mean of B and $\phi_{t_0}^t(B)$ are merely the geometric centroids of the respective sets. Further we note that $(\bar{\xi}_1, \bar{\xi}_2) \neq \phi_{t_0}^t(\bar{x}_1, \bar{x}_2)$, the image of the mean need not be the mean of the image set.

5.1. Computation of σ_i for autonomous and periodic vector fields

It is natural to expect the Perron–Frobenius operator to play a role in the computation of the covariance FTLE. The operator $\mathcal{P}_{t_0}^t$ can be found using a suitable set of K time intervals, $[t_0, t_1], [t_1, t_2], \dots, [t_{K-1}, t_K]$, where $t_K = t$, as the composition,

$$\mathcal{P}_{t_0}^{t_K} = \mathcal{P}_{t_{K-1}}^{t_K} \dots \mathcal{P}_{t_1}^{t_2} \mathcal{P}_{t_0}^{t_1}. \tag{20}$$

Let f be a uniform density function supported on a set B . Then, as before, $\mathcal{P}_{t_0}^{t_K}$ maps f under the action of the flow map to $\mathcal{P}_{t_0}^{t_K} f$, i.e., $f \mapsto \mathcal{P}_{t_0}^{t_K} f$. For time-independent, or time-periodic vector fields with period Δt , this calculation becomes particularly easy. A Δt -periodic vector field defined by the time-dependent vector field,

$$\dot{\mathbf{x}} = \mathbf{F}(\mathbf{x}, t)$$

is such that $\mathbf{F}(\mathbf{x}, t + \Delta t) = \mathbf{F}(\mathbf{x}, t)$. The associated flow map can be denoted by $\phi_{t_0}^t(\mathbf{x})$, which takes points \mathbf{x} at time t_0 to their location at time t is periodic in the following sense,

$$\phi_{t_0}^t(\mathbf{x}) = \int_{t_0}^t F(\mathbf{x}, \tau) d\tau = \int_{t_0+\Delta t}^{t+\Delta t} F(\mathbf{x}, \tau + \Delta t) d\tau = \phi_{t_0+\Delta t}^{t+\Delta t}(\mathbf{x}).$$

Now consider an initial density f supported on the set B at time t_0 . The image of the density at time t is given by

$$\mathcal{P}_{t_0}^t f = \int_{(\phi_{t_0}^t)^{-1}(B)} f d\mu = \int_{(\phi_{t_0+\Delta t}^{t+\Delta t})^{-1}(B)} f d\mu = \mathcal{P}_{t_0+\Delta t}^{t+\Delta t} f. \tag{21}$$

When we are interested in the operator over integer multiples of the vector field period, i.e., $t_K = t_0 + K\Delta t$, where, using $t_i = t_{i-1} + \Delta t$ for $i = 1, \dots, K$, we get

$$\mathcal{P}_{t_0}^{t_K} = (\mathcal{P}_{t_0+\Delta t}^{t_0+\Delta t})^K. \tag{22}$$

In the case of the time reversible matrix approximation for \mathcal{P} , we have $(P_r)_{t_0}^{t_K} \approx ((P_r)_{t_0+\Delta t}^{t_0+\Delta t})^K$. This method of approximating $\mathcal{P}_{t_0}^{t_K}$ avoids long time integration of trajectories. The projection of a uniform density function supported on the set B_i is the row n -vector,

$$\pi f = \mathbf{b}^i = [0, 0, \dots, 1/\mu(B_i), \dots, 0, 0], \tag{23}$$

with the only nonzero entry in the i th slot, which evolves to the row N -vector $\mathbf{b}^i(t_K)$ given by,

$$\mathbf{b}^i(t_K) \approx \mathbf{b}^i(t_0)(P_{t_0+\Delta t}^{t_0+\Delta t})^K. \tag{24}$$

The R.H.S of the above equation is merely the i th row of the matrix $(P_{t_0+\Delta t}^{t_0+\Delta t})^K$ divided by $\mu(B_i)$. The covariance of this set can be found from the i th row of $(P_{t_0+\Delta t}^{t_0+\Delta t})^K$ as follows,

$$I(\mathbf{b}^i(t_K)) \approx \frac{1}{\mu(B_i)} \begin{bmatrix} \sum_{j=1}^n ((\bar{\zeta}_1^j - \bar{\zeta}_1^i)^2 (P_{t_0}^{t_K})_{ij}) & \sum_{j=1}^n ((\bar{\zeta}_1^j - \bar{\zeta}_1^i)(\bar{\zeta}_2^j - \bar{\zeta}_2^i)(P_{t_0}^{t_K})_{ij}) \\ \sum_{j=1}^n ((\bar{\zeta}_1^j - \bar{\zeta}_1^i)(\bar{\zeta}_2^j - \bar{\zeta}_2^i)(P_{t_0}^{t_K})_{ij}) & \sum_{j=1}^n ((\bar{\zeta}_2^j - \bar{\zeta}_2^i)^2 (P_{t_0}^{t_K})_{ij}), \end{bmatrix} \tag{25}$$

where $(\bar{\zeta}_1^j, \bar{\zeta}_2^j)$ are the centers (mean values) of each of the boxes, B_j , and $(\bar{\zeta}_1^i, \bar{\zeta}_2^i) = \sum_{j=1}^n ((\bar{\zeta}_1^j, \bar{\zeta}_2^j)(P_{t_0}^{t_K})_{ij})$. Intuitively the uniformly distributed points in box B_i are mapped into up to n boxes by the flow map $\phi_{t_0}^{t_K}$, say boxes B_j, B_k and B_m as shown in Fig. 10. If the number of points that are mapped into each of the three boxes are N_j, N_k and N_m , then each of the three sets $B_j \cap \phi_{t_0}^{t_K}(B_i), B_k \cap \phi_{t_0}^{t_K}(B_i)$ and $B_m \cap \phi_{t_0}^{t_K}(B_i)$ are approximated by N_j, N_k and N_m uniformly distributed points in the boxes B_j, B_k and B_m . The mean or average of these dispersed points is $(\bar{\zeta}_1^i, \bar{\zeta}_2^i)$. Then,

$$\mathbf{b}^i(t_K) = \frac{1}{\mu(B_i)} [0, \dots, (P_{t_0}^{t_K})_{ij}, 0, \dots, (P_{t_0}^{t_K})_{ik}, 0, \dots, (P_{t_0}^{t_K})_{im}, \dots 0], \tag{26}$$

with nonzero values in rows j, k and m . The mean or center of this set is given by $(\bar{\zeta}_1^i, \bar{\zeta}_2^i)$. Proceeding thus, the covariance FTLE for each of the boxes in the domain can be found from (25). As we noted earlier, $P_{t_0}^{t_K} \approx (P_{t_0+\Delta t}^{t_0+\Delta t})^K$ and this is reflected in the approximation $\phi_{t_0}^{t_K}(B) \approx \frac{1}{\mu(B_i)} (P_{t_0}^{t_K})_{ij} \mathcal{X}_{B_j} \cap (P_{t_0}^{t_K})_{ik} \mathcal{X}_{B_k} \cap (P_{t_0}^{t_K})_{im} \mathcal{X}_{B_m}$.

6. Examples

We apply the method the covariance FTLE to three examples and compare the results with those obtained from computations of the standard FTLE and AIS. The first two are periodic vector fields and the third is the atmospheric flow on a constant pressure surface, an aperiodic, finite-time vector field.

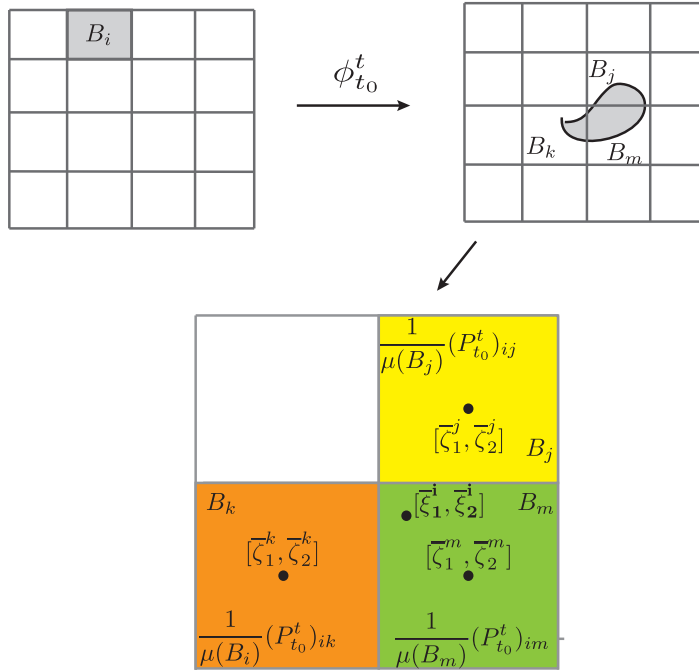


Fig. 10. Illustration of the calculation of the covariance, $I(v^t(t))$ in (25). The initial uniform density function $\frac{1}{\mu(B_i)}$ supported on the set B_i is mapped to the density function $P_{t_0}^t(B_i)$ which is approximated by three uniform density functions $\frac{1}{\mu(B_j)}(P_{t_0}^t)_{ij}$, $\frac{1}{\mu(B_k)}(P_{t_0}^t)_{ik}$ and $\frac{1}{\mu(B_m)}(P_{t_0}^t)_{im}$ supported on the sets B_j, B_k and B_m , respectively, for $t = t_0 + K\Delta t$, where K is an integer and Δt is the period of the underlying vector field.

6.1. Lid-driven cavity flow

The first example we consider is the lid-driven cavity flow in which mixing has been recently studied by the method of AISs in [28–30]. The model has been extensively studied in [44] and is considered here as the first example because of its simple piecewise steady velocity field, which is described by the stream function

$$\psi(x, y) = \sum_{n=1}^2 U_n C_n f_n(y) \sin\left(\frac{n\pi x}{a}\right) \tag{27}$$

defined on the domain $M = [0, a] \times [-b, b] \subset \mathbb{R}^2$ for time $t \in [k\tau_f, (k + 1)\tau_f/2]$, for integer k , where

$$f_n = \frac{2\pi y}{a} \cosh\left(\frac{n\pi b}{a}\right) \sinh\left(\frac{n\pi y}{a}\right) - \frac{2\pi b}{a} \sinh\left(\frac{n\pi b}{a}\right) \cosh\left(\frac{n\pi y}{a}\right)$$

and

$$C_n = \frac{a^2}{2n\pi^2 b} \left[\frac{a}{2n\pi b} \sinh\left(\frac{2n\pi b}{a}\right) + 1 \right]^{-1}.$$

For time $t \in [(k + 1)\tau_f/2, (k + 1)\tau_f]$, the sign of the velocity term U_1 is changed. This reflects the streamlines about $x = a$ after every time $\tau_f/2$.

Using symmetry arguments given in [44], a specific ratio of the magnitudes of the terms U_2/U_1 along with a fixed value of the period of the velocity field, τ_f , is found such that it generates three period-3 fixed points in the domain $[0, a] \times [-b, b]$. The specific values of the constants that use are from [44]: $U_1 = -1$, $U_2 = 0.841298$, $\tau_f^*/2 = 4.740202$, and the domain $[0, a] \times [-b, b] = [0, 6] \times [-1, 1]$. A perturbation of the half-period of the velocity field away from the critical value of $\tau_f^*/2 = 4.740202$ destroys the fixed points. The method of AISs was used in [28–30] to study mixing for different values of the perturbed half-period. Since our main interest here is to compare the AISs with coherent sets, we choose a single case, a specific value of half-period $\tau_f/2 = 4.848$ for our study.

The domain is discretized into $120 \times 40 = 4800$ equal-sized square boxes, each box containing 100 uniformly distributed points. The time-reversible Perron–Frobenius matrix P_r for a duration equal to τ_f , i.e., from $t = 0$ to $t = \tau_f$ is found from (2)–(4). Fig. 11 shows the second right eigenvector v^2 of the matrix $(P_r)_0^{\tau_f}$. The sign of the eigenvector is positive in a portion of the domain and negative in the remainder. As explained in Section 2.1, the zero contour of the second eigenvector in Fig. 11 forms the boundary between the two AISs. The two AISs are shown in Fig. 11(b), in which the three black blobs correspond to

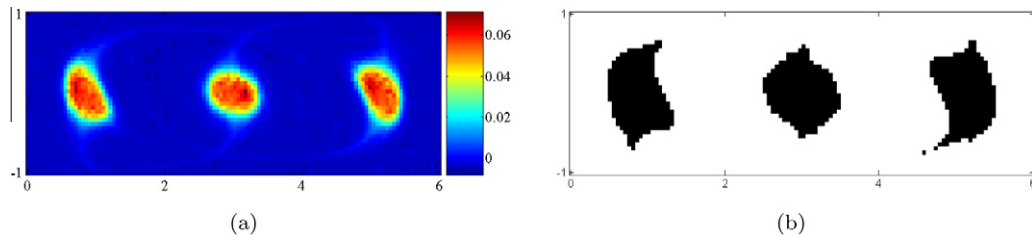


Fig. 11. (a) Second right eigenvector v^2 for the lid-driven cavity flow and (b) AIS obtained from positive part of the second eigenvector of P_r , in black. The phase space complement, in white, is also an AIS.

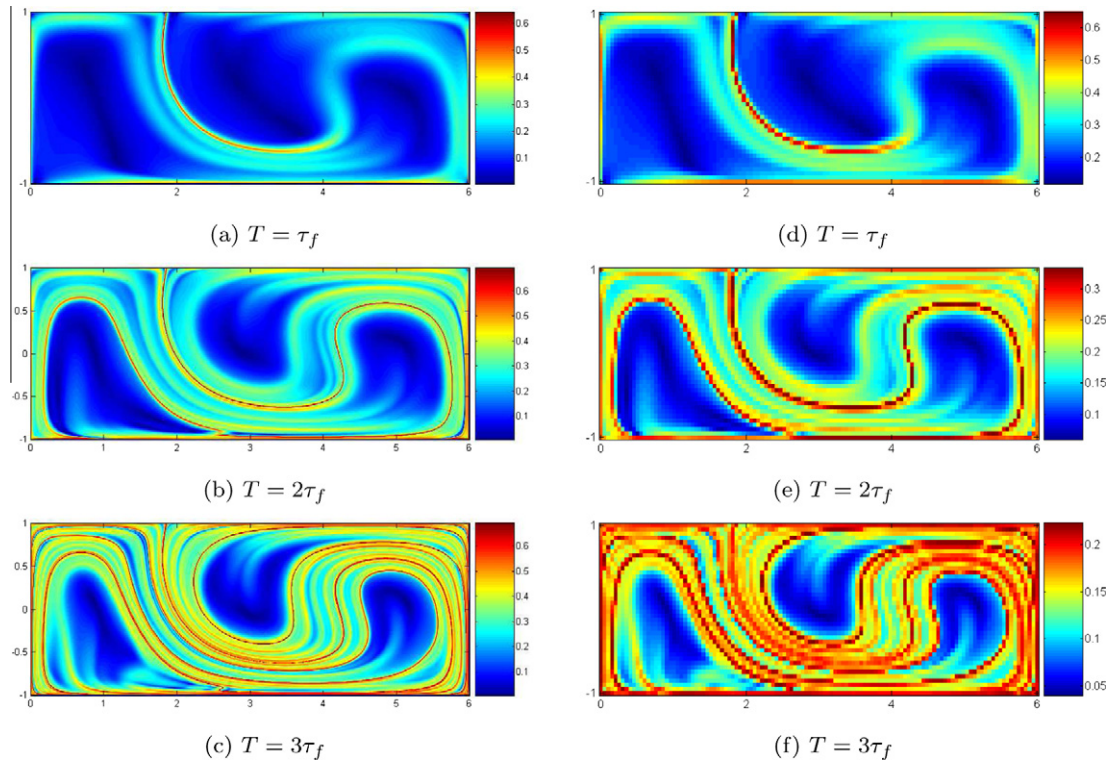


Fig. 12. FTLE from $t = 0$ to $t = T$ for the lid-driven cavity flow, computed using the conventional line element approach (a)–(c), and using the covariance based approach (d)–(f), for the given values of T .

the positive part of the second eigenvector, and the phase space complement (in white), corresponds to the negative part. The FTLE field obtained from the conventional line stretching method (13) for different integration times are shown in Fig. 12(a)–(c). The covariance FTLE field for this system can be calculated either directly (18) or using the PF operator (25). The FTLE field obtained from the direct covariance method using the same discretization as for the AISs is shown in Fig. 12(d)–(f). The FTLE field $\sigma_I(0, 3\tau_f)$ calculated from $((P_r)_0^{\tau_f})^3$ using (25) is shown in Fig. 13.

Comparing the results in Fig. 12(a)–(c) and (d)–(f) we find that the covariance approach of computing the FTLE agrees qualitatively with the standard FTLE. This agreement is in the structure of the FTLE field only (e.g., the high ridges, or LCSs) and not in the exact values of the FTLEs. The FTLE fields in Fig. 12(a)–(c) look finer than those in Fig. 12(d)–(f) and, even though both used the same 4800×100 (initial) points. This is because the regions of high deformation in 12(d)–(f) are identified by boxes of non-zero measure, while for the FTLE computed by the conventional line stretching method the ridges in the FTLE field are codimension one, i.e., zero measure. However, the coarse-looking FTLE field computed by our new approach measures the deformation of sets, including higher order deformations, rather than that of line elements. Comparing the FTLE fields in Figs. 12(f) and 13, we note that the values of the FTLE are underestimated by (25) though the qualitative features of the FTLE field are the same.

Coherent sets are obtained by setting an arbitrary threshold of $\sigma_I^{\max} = 0.06$ on the FTLE field obtained by the direct covariance method. These coherent sets are shown in black in Fig. 14(a). These sets do not disperse nor mix quickly with the rest of

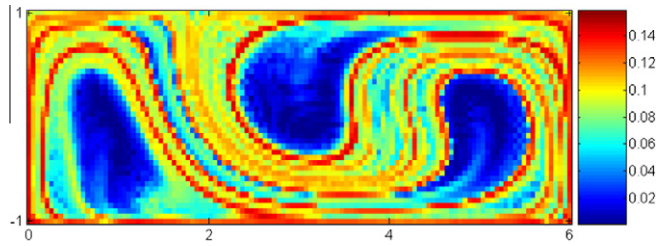


Fig. 13. FTLE field $\sigma_t(0, 3\tau_f)$ calculated from $(P_0^{\tau_f})^3$ using (25).

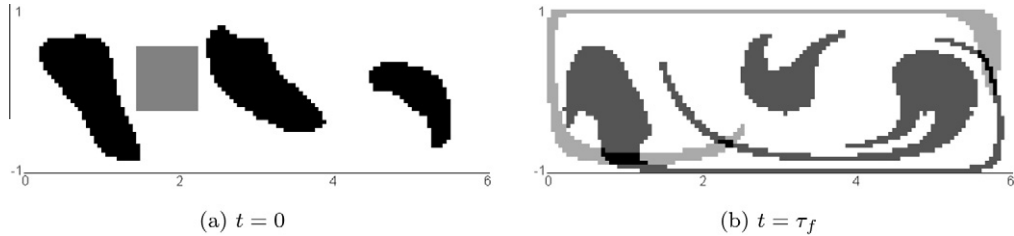


Fig. 14. Coherent sets (black) do not disperse significantly while non-coherent sets (gray) do. In (a) the three coherent sets (black) identified by our $\sigma_t \leq 0.06$ criterion and a non-coherent set (gray) are shown at $t = 0$. At $t = \tau$, the non-coherent set disperses significantly more than the coherent sets. Figure (b) also shows mixing between the ‘particles’ of the non-coherent set with those of the coherent sets.

the domain as non-coherent sets do. An example non-coherent set (gray) is also shown in Fig. 14(a). The non-coherent set disperses and mixes with the rest of the domain quickly while the coherent sets (in black) do not, as shown in Fig. 14(b).

We note that the coherent sets we calculate are not exactly the same as the AISs shown in Fig. 11(b). However the interpretation of almost invariance using the second eigenvector of P_r can be problematic when the higher eigenvalues are close to the second eigenvalue. We computed the first 6 eigenvalues and vectors of the discretized Perron–Frobenius operator. The values are $\lambda_2 = 0.9925$, $\lambda_3 = 0.9829$, $\lambda_4 = 0.9516$, $\lambda_5 = 0.9473$ and $\lambda_6 = 0.9434$, with the corresponding eigenvectors v^3 and v^4 shown in Fig. 15 for comparison.

The invariance of a set B is given by $\rho_{M_f}(B)$ in (5) and the eigenvalues and eigenvectors of P_r provide an approximate way to divide the domain into two almost invariant sets, [8,11]. However if the eigenvalues of P are close to each other in magnitude, one can obtain other AISs that are slightly less invariant than those obtained from the second eigenvector. From an application point of view the eigenvectors, v^k , where $k \geq 3$, are perhaps as important as the second eigenvector. Moreover linear combinations of the eigenvectors can produce a family of AISs that could be the most physically important. This is the case in earlier work [45] where eigenvectors ranging from the 11th to 39th were used to identify optimally almost invariant sets. We can only conjecture that our FTLE approach identifies a particular combination of the eigenvectors of P_r corresponding to closely spaced eigenvalues.

Next we show numerically that the coherent sets in Fig. 14(a) remain almost coherent under the action of the flow map. We evolve unit density functions supported on the coherent sets and the AISs. We take a set of uniformly distributed particles in the coherent sets (Fig. 14(a)) and AISs (Fig. 11(b)) respectively and advect them. Fig. 16 shows the evolution of the coherent and AISs. The coherent and the AISs in fig. 16(a) and (e) can be thought of as sets containing a tracer of unit concentration. Fig. 16(b)–(d) show that the coherent sets identified in 16(a) do not disperse significantly with time. The $\sigma_t(0, \tau_f)$ values of each of the three sets from left to right in Fig. 16(b) are 0.0032, 0.0056, and 0.0026, which shows that the sets do not disperse significantly. For comparison the non-coherent set shown in Fig. 14 spreads quickly even when $t = \tau_f$ with $\sigma_t(0, \tau_f) = 0.1314$. The $\sigma_t(0, \tau_f)$ values of the AIS in Fig. 16(f) are 0.0018, 0.0075 and 0.0017. These values are of the same order of magnitude to those of the coherent sets identified by the σ_t criterion. The coherent sets identified by the $\sigma_t(0, \tau_f)$

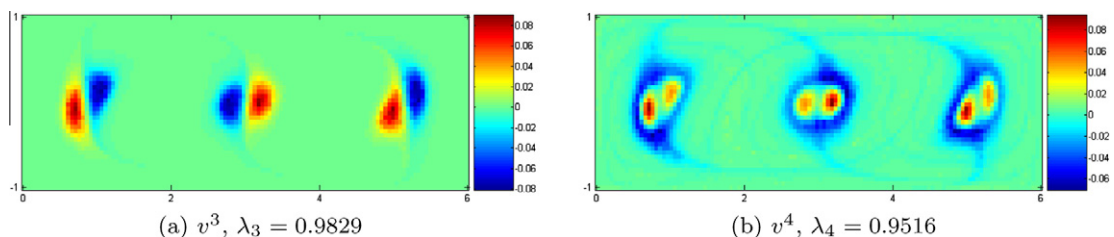


Fig. 15. Higher eigenvectors v^3 and v^4 .

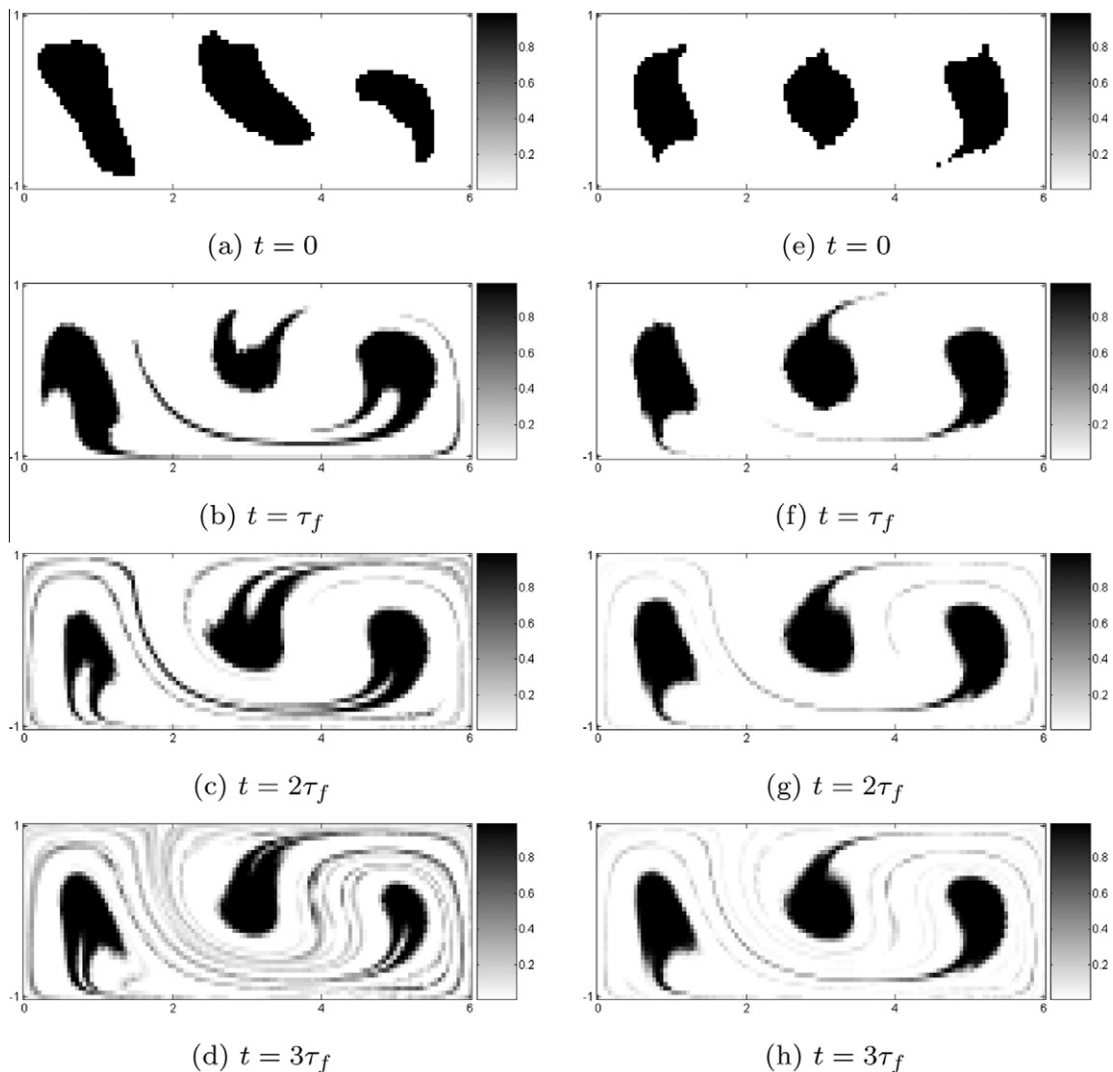


Fig. 16. Comparison of the $\sigma_I(0, \tau_f)$ -coherent sets (left) and eigenvector-based AISs (right) for the lid-driven cavity flow, i.e., the top sets are identical to those in Figs. 14(a) and 11(b).

remain coherent beyond $t = \tau_f$. The $\sigma_I(0, 3\tau_f)$ values of each of the three sets in Fig. 16(d) are 0.0265, 0.0352, and 0.0434, which are still smaller than the $\sigma_I(0, \tau_f)$ of the non-coherent set. In fact, at $t = 3\tau_f$ the coherent sets have almost the same qualitative structure as the AISs in 16(h). The structure of the coherent sets is qualitatively the same as obtained by setting a threshold on the value of the FTLE in Fig. 12. The identification of the coherent sets with AISs gets better with increasing time as in Fig. 16(d) and (h).

6.2. Double gyre flow

The lid-driven cavity flow in the previous section is not only piecewise smooth, but piecewise time independent. Here we consider the double gyre flow with the same parameters mentioned in Section 3. The domain is discretized into 50,000 equal-sized square boxes of dimensions 0.005×0.005 , with each box containing 625 uniformly distributed points. The FTLE fields obtained for an integration period $T = 10$, using the direct method of covariance (18) is shown in Fig. 17(a). Fig. 17(a) shows the FTLE field obtained using $(P_{t_0}^{t_0+\Delta t})^{10}$ and (25). Here again we note that the numerical values of $\sigma_I(B_i)$ obtained from both the methods are only approximately equal. However the use of the PF operator produces a smooth FTLE field.

Using the same discretization for the Perron–Frobenius operator P of the flow map as for the covariance FTLE, we found the eigenvalues of P to be $\lambda_2 = 0.9997$, $\lambda_3 = 0.9995$, $\lambda_4 = 0.9987$, $\lambda_5 = 0.9981$ and $\lambda_6 = 0.9971$. The eigenvalues for this problem are very closely spaced and here we find that the eigenvectors v^2 and v^3 , shown in Fig. 18, have a similar structure as do the eigenvectors v^4 to v^6 (not shown). It has been pointed out in [46] that in problems where there exist a cluster of

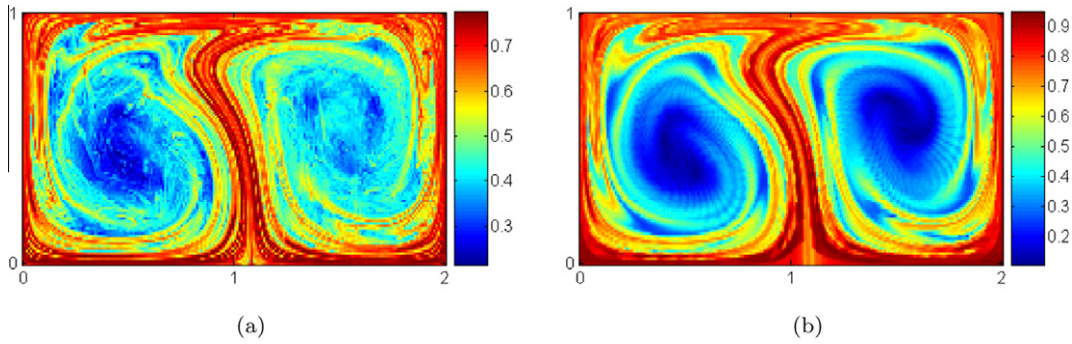


Fig. 17. (a) FTLE fields for the double gyre flow obtained from the direct covariance FTLE method (18) and (b) using PF operator (25) for an integration time of $T = 10$.

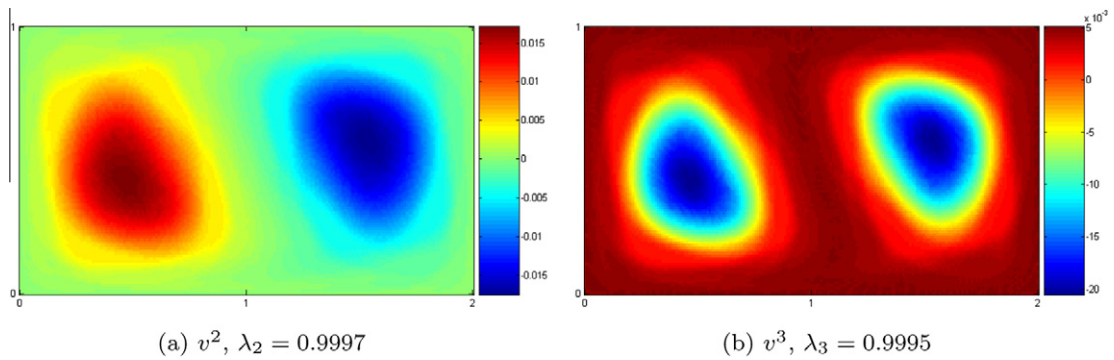


Fig. 18. The eigenvectors, v^2 and v^3 , of the $(P_T)_0^T$ for the double gyre flow.

eigenvalues close to 1, the computation of the eigenvectors are sensitive to the discretization of the domain. Observing the plots of the eigenvectors v^2 and v^3 in Fig. 18 we can see that almost invariant sets obtained by using the zero contour of the eigenvectors v^3 are almost the same as the almost invariant sets obtained from v^2 .

By setting a threshold $\sigma_l^{\max} = 0.6$, we obtain two coherent sets. The positive part of v^2 is almost the entire left half, so we set a threshold of 0.001 for the absolute value of v^2 to obtain the AISs, as was done in [42]. The coherent sets identified by the new FTLE approach and the AIS identified by the second eigenvector of the Perron–Frobenius operator for the double gyre flow are shown in Fig. 19. We find that the coherent sets identified by both the methods are roughly the same, though the method of AIS defines a compact boundary for the sets. But in this case the compact boundary is perhaps arbitrary since the eigenvectors corresponding to higher eigenvalues identify different (overlapping) sets.

6.3. Atmospheric flow

We apply the same concept of coherent sets using the covariance FTLE to atmospheric flow, a time-dependent aperiodic flow, defined by a meteorological velocity data set. Optimal coherent sets in the oceans and the atmosphere on continental

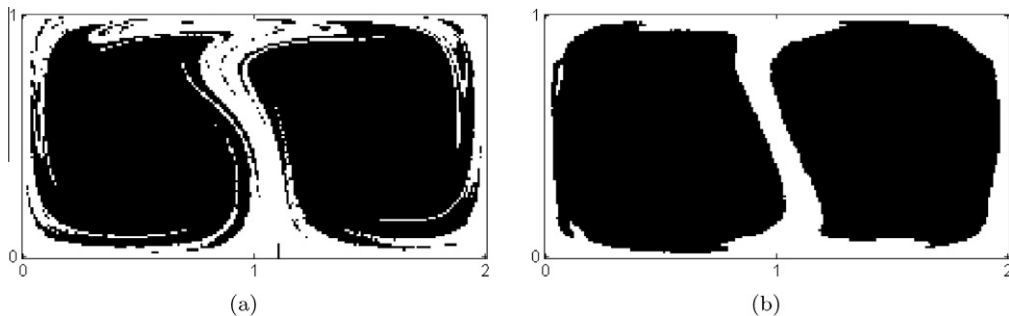


Fig. 19. (a) Coherent sets and (b) AISs in the double gyre flow.

scales for long periods of time were investigated in [47,45]. We apply our method of covariance-based FTLE to identify sets that persist for a few hours to days. The domain of the atmospheric flow in our example is the eastern United States. The velocity field is obtained from the North American Mesoscale (NAM)-12 km Weather Research and Forecasting (WRF) Model reanalysis data. This data set defines velocity data on a grid over North America at 3 h intervals, at points that are roughly spaced 12.5 km apart. The resulting domain is highly leaky, often with more than a quarter of trajectories escaping the domain in 24 h. For time scales of a few hours to a few days, the problem of identifying coherent sets in such a leaky domain is not possible using the AIS approach. Therefore, we must apply our definition of FTLE and coherent sets to qualitatively identify coherent sets that persist for a few hours.

Another motivation to study coherent sets in the atmosphere is to investigate the possible role played by punctuated changes in the concentration of a tracer (see, e.g., [48]). A punctuated change is a rapid temporal change in the concentration of a passive or active chemical or biological tracer at a sampling point. In [21], punctuated changes of the concentration of fungi of the genus *Fusarium* in 73 aerial samplings were shown to be correlated to the motion of repelling and attracting LCS. Here we focus on only one important series of samples [48], which provides a good test case for our formulation of coherent sets. It was established that the *Fusarium* concentration in the atmosphere at 100 m altitude at the sampling location (37.1971°N latitude and 80.5738°W longitude) was high; 12.3 spores/m₃ and 7.5 spores/m₃; at 14:00 and 15:00 UTC, respectively on 1 May 2007 while at 20:15 UTC and on the same day it was low; 2.1 spores/m₃ and 1.2 spores/m₃ respectively (all times listed will be UTC from now on). The identification of high and low concentration is based on the average concentration of the spores found in the lower atmosphere throughout the year. The reader is referred to [21] for details on the calculation of spore concentration from raw data. We show that two distinct sets were sampled leading to the variation in the spore count. For our computations we used the NAM-12 km WRF reanalysis data on a 900 mb pressure surface (corresponding to the height of the sampling location) in a domain that is 600 km × 600 km centered around the geographical location of the sampling point (the circle in the center of Figs. 20 and 21). We discretized the domain into 14,400 square boxes each of size 10 km × 10 km and containing 100 uniformly spaced points and integrated all the 1.44×10^6 points for a duration of 24 h. The covariance-based FTLE is shown in Fig. 20.

We used a threshold value of 0.1/hr for the covariance FTLE field to obtain coherent sets at 09:00 on 1 May 2007. The evolution of these coherent sets in forward time is shown in Fig. 21. From Figs. 20 and 21 it is clear that coherent sets once identified (09:00), remain coherent for many hours. Further the evolution of coherent sets in forward time is such that they coincide with the sets of a low FTLE value in future time. In Fig. 21(a) and (b) a coherent set persists over the sampling point. The movement of this coherent set away from the sampling point leads to sampling a non-coherent set at 15:00 and the resulting spike in the concentration of the *Fusarium* spores. The sampling of another distinct coherent set at 21:00 on 1 May and 00:00 on 2 May results in a fall in the concentration of the *Fusarium* spores. While we did not collect any samples on 1 May 2007 before 15:00, the samples collected at 15:00 on the previous day, 30 April 2007, show a low concentration of the spores. We hypothesize that the concentration of the spores would have been low between 09:00 and 12:00 on 1 May, since a distinct coherent set was sampled at these times. These results show that finite-time coherent sets may play an important role in punctuated changes of a tracer in the atmosphere. Computations of coherent sets at a finer temporal and spatial scale are necessary to confirm if different coherent sets were sampled between 14:00 and 15:00.

7. Conclusion and discussion

In complex time-dependent flows, stretching and folding can be high, and these play an important role in mixing and transport. The standard FTLE, when calculated accurately, quantifies only the time averaged stretching in a local neighborhood of reference trajectories. Moreover there are computational difficulties in accomplishing this calculation accurately for vector fields based on numerical data, leading to spurious values of the FTLE. For this reason the classic definition of the FTLE often generates spurious values of FTLEs. The covariance-based method of computing the FTLE, introduced in this paper, does not use the linearized equations of a flow map. Thus arbitrary integration times that produce nonlinear stretching and folding of material lines do not affect our computations. Moreover our redefinition of the FTLE is a set based definition and identifies the dispersion of sets of non-zero measure. The classic FTLE is a time-varying scalar field $\sigma(\mathbf{x}, t_0, t)$, defined on a set of grid points, which calculates linearized time-averaged stretching for material elements initially around the grid points. From this it is not possible to identify how much a set of positive measure in the domain stretches or disperses. With our set oriented approach we can calculate the FTLE of any set B which is composed of small boxes B_i . The probabilistic covariance matrix can be interpreted geometrically as the moment of inertia of a set which gives a measure of stretching and dispersion in phase space. Thus the proposed set oriented definition of the FTLE offers a straightforward connection between the evolution of probability densities and finite time stretching experienced by material lines. The set oriented FTLE has the same value as the standard FTLE when the growth of a perturbed trajectory is linear, as shown with sample calculation in Section 4. Thus our definition is an extension of the standard FTLE and can also be used in applications where the standard FTLE is used. While the modified definition of the FTLE has a probabilistic interpretation, it suffers from the drawback of using the second moments of a density function. Thus one cannot pose the question of finding an optimal union of coherent sets as an eigenvalue problem. The computational cost of a brute-force search amongst the density functions to identify an optimal union of coherent sets is prohibitive. We leave the development of a systematic method to identify optimal coherent sets from the σ_t field to future work.

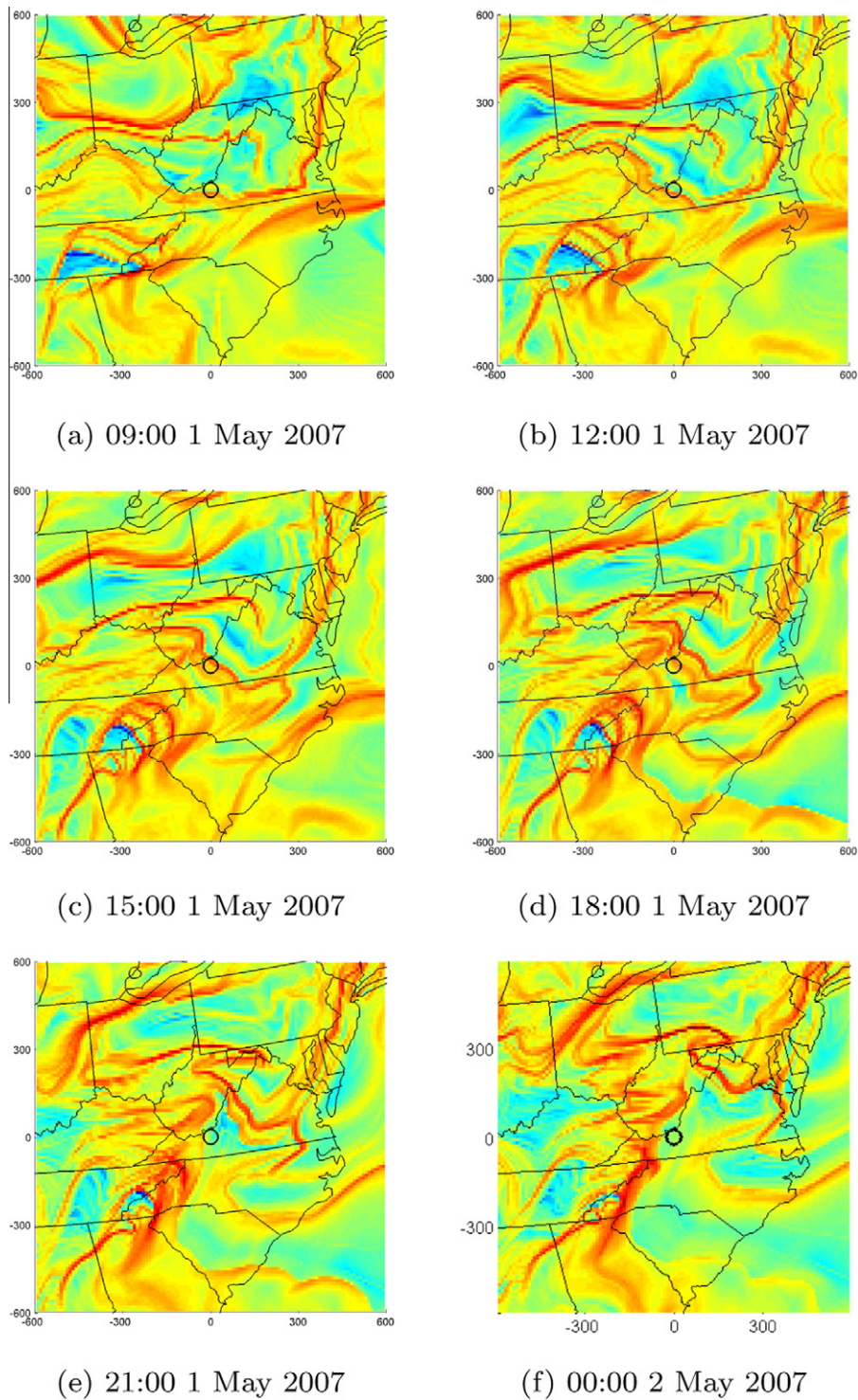


Fig. 20. Covariance-based FTLE field for a duration of $T = 24$ h for initial starting times (a)–(f). Red regions represent sets with high covariance FTLE and blue regions represent sets with low covariance FTLE. The sampling region is represented by the open circle at the middle of each panel. (For interpretation of the references to colour in this figure legend, the reader is referred to the web version of this article.)

We identified coherent sets by setting a threshold value on the covariance-based FTLE, σ_l . Viewing σ_l as a graph over the domain, the coherent sets are the ‘valleys’, and are naturally separated from one another by the ‘ridges’ of high σ_l , providing a concrete link between the framework of coherent sets and that of codimension one Lagrangian coherent structures. While

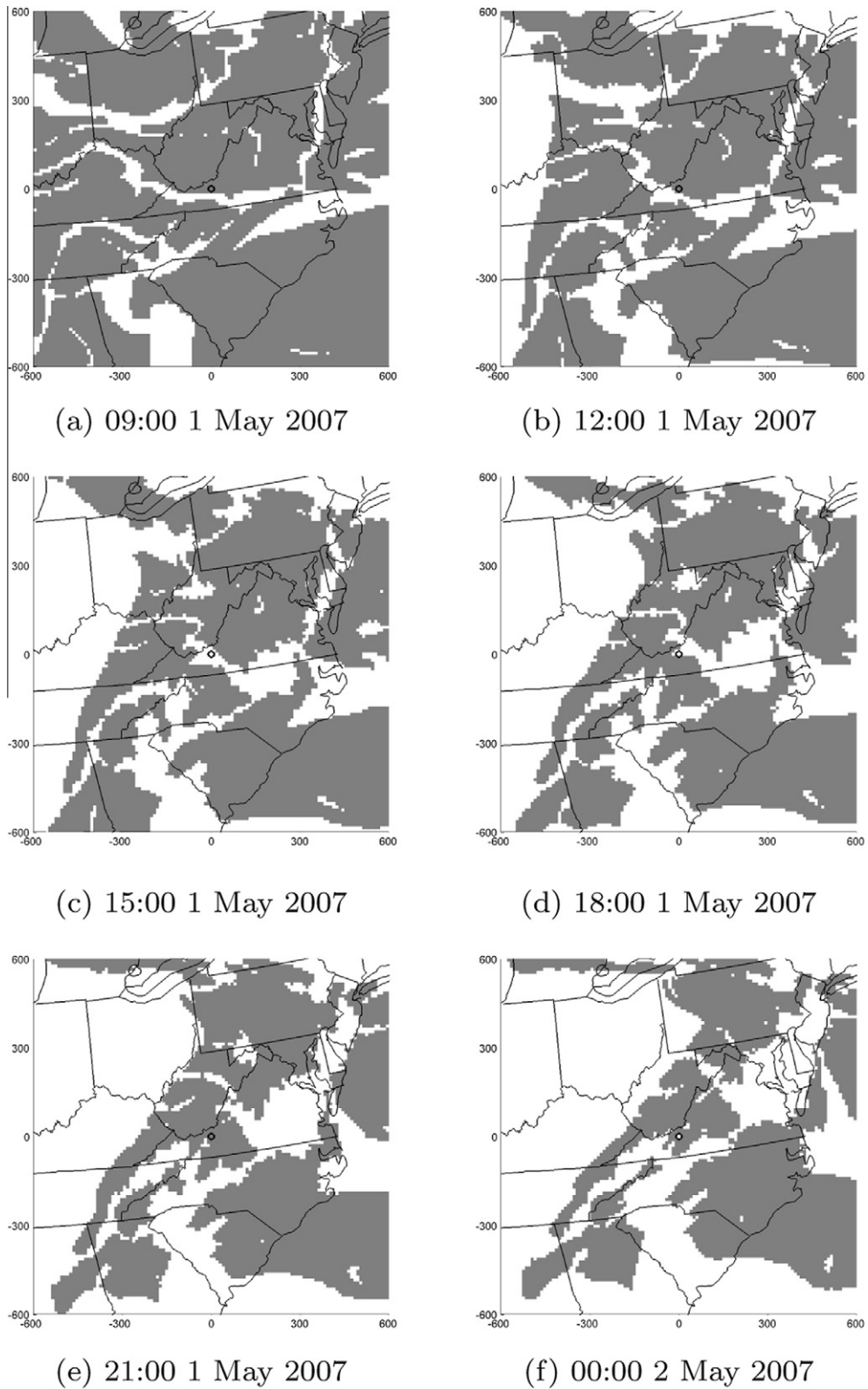


Fig. 21. Evolution of the coherent sets obtained by the FTLE method for an integration time of 24 h. The coherent sets (gray regions) were identified from the covariance FTLE field at the initial time (Fig. 20(a)) by setting a threshold of $\sigma_i^{\max}(0, \tau) = 0.1/h$. Figures (b)–(f) show the evolution of these sets. The set boundaries correspond roughly with the ridges of high FTLE in Fig. 20, but the agreement deteriorates with time.

using a threshold value for the FTLE may not identify optimally coherent sets, it does offer a simple way to identify finite-time coherent sets in a heuristic manner in complex time-dependent flows. We point out that for many time-dependent systems this is not a serious drawback of the method because it is not obvious that time-dependent systems always admit a partitioning into two optimally coherent sets. This was demonstrated with examples related to mixing and transport in fluid flows. In the first two examples, the lid-driven cavity flow and the double gyre flow, our method provided a good approximation of coherent sets when compared with the AIS. The third example, the case of atmospheric flow, presents many difficulties due to the complex time-varying nature of the flow, the highly translating nature of the flow map, and the leaky domain. While this situation renders the method of AIS impossible, our method still identified approximate finite-time coherent sets. We view this method as providing a first guess to a systematic optimization procedure to identify maximally coherent sets in time dependent flows.

As a specific application, the definition of coherent sets using the covariance FTLE should be useful to track and predict the movement of sets of tracers such as pollutants, pathogens, and other passive chemical and biological tracers, in environmental flows such as those found in the atmosphere, oceans, and lakes.

Acknowledgments

We wish to thank the following colleagues for helpful discussions and comments: Mohsen Gheisarieha, Piyush Grover, Mirko Hessel-von Molo, Pankaj Kumar, and Mark Stremmler. This material is based upon work supported by the National Science Foundation under Grant Nos. 0919088, 1100263, and 1150456. Any opinions, findings, and conclusions or recommendations expressed in this material are those of the authors and do not necessarily reflect the views of the National Science Foundation.

References

- [1] Wiggins S. Chaotic transport in dynamical systems. Interdisciplinary applied mathematics. New York: Springer; 1993.
- [2] Ide K, Small D, Wiggins S. Distinguished hyperbolic trajectories in time dependent fluid flows: analytical and computational approach for velocity fields as data sets. *Nonlinear Process Geophys* 2002;9:237–63.
- [3] Wiggins S. The dynamical systems approach to Lagrangian transport in oceanic flows. *Ann Rev Fluid Mech* 2005;37:295–328.
- [4] Shadden SC, Lekien F, Marsden J. Definition and properties of Lagrangian coherent structures from finite-time Lyapunov exponents in two-dimensional aperiodic flows. *Physica D* 2005;212:271–304.
- [5] Lekien F, Shadden SC, Marsden J. Lagrangian coherent structures in n -dimensional systems. *J Math Phys* 2007;48.
- [6] Haller G. Lagrangian coherent structures and the rate of strain in a partition of two-dimensional turbulence. *Physica D* 2011;240:574–98.
- [7] Haller G. A variational theory of hyperbolic Lagrangian Coherent Structures. *Phys Fluids A* 2001;13:3368–85.
- [8] Dellnitz M, Junge O. On the approximation of complicated dynamical behavior. *SIAM J Numer Anal* 1998;36:491–515.
- [9] Dellnitz M, Junge O, Koon WS, Lekien F, Lo MW, Marsden JE, Padberg K, Preis R, Ross SD, Thiere B. Transport in dynamical astronomy and multibody problems. *Int J Bifurcat Chaos* 2005;15:699–727.
- [10] Dellnitz M, Junge O, Lo MW, Marsden JE, Padberg K, Preis R, Ross SD, Thiere B. Transport of Mars-crossing asteroids from the quasi-Hilda region. *Phys Rev Lett* 2005;94:231102.
- [11] Froyland G, Dellnitz M. Detecting and locating near-optimal almost-invariant sets and cycles. *SIAM J Sci Comput* 2003;24:1839–63.
- [12] Froyland G, Lloyd S, Santitissadeekorn N. Coherent sets for nonautonomous dynamical systems. *Physica D* 2010;239:1527–41.
- [13] Froyland G, Santitissadeekorn N, Monahan A. Transport in time-dependent dynamical systems: finite time coherent sets. *Chaos* 2010;20:043116.
- [14] P.C. Du Toit, Transport and separatrices in time dependent flows. Ph.D. thesis, California Institute of Technology; 2010.
- [15] Dellnitz M, Hohmann A, Junge O, Rumpf M. Exploring invariant sets and invariant measures. *Chaos* 1997;7:221.
- [16] Pierrehumbert RT. Chaotic mixing of tracers and vorticity by modulated traveling Rossby waves. *Geophys. Astrophys. Fluid Dyn.* 1991;58:285–320.
- [17] Pierrehumbert RT. Large-scale horizontal mixing in planetary atmospheres. *Phys. Fluids* 1991;3A:1250–60.
- [18] Bowman K. Manifold geometry and mixing in observed atmospheric flows. Unpublished manuscript. Available from: http://geotest.tamu.edu/userfiles/213/manifold_geometry.pdf.
- [19] Coulliette C, Lekien F, Paduan JD, Haller G, Marsden J. Optimal pollution mitigation in Monterey bay based on coastal radar data and nonlinear dynamics. *Environ. Sci. Technol.* 2007;41:6562–72.
- [20] Tallapragada P, Ross SD. Particle segregation by Stokes number for small neutrally buoyant spheres in a fluid. *Phys. Rev. E* 2008;78.
- [21] Tallapragada P, Ross SD, Schmale DG. Lagrangian coherent structures are associated with fluctuations in airborne microbial populations. *Chaos* 2011;21:033122.
- [22] Lekien F, Ross SD. The computation of finite-time Lyapunov exponents on unstructured meshes and for non-Euclidean manifolds. *Chaos* 2010;20:017505.
- [23] Tang W, Mathur M, Haller G, Hahn DC, Ruggiero FH. Lagrangian coherent structures near a subtropical jet stream. *J. Atmos. Sci.* 2010;67:2307–19.
- [24] Bowman K. Observations of fine-scale transport structure in the upper troposphere from the high-performance instrumented airborne platform for environmental research. *J. Geophys Res*: 112.
- [25] Wilson M, Peng J, Dabiri JO, Eldredge JD. Lagrangian coherent structures in low Reynolds number swimming. *J. Phys. Condensed Matter* 2009;21:204105.
- [26] Harrison CS, Glatzmaier GA. Lagrangian coherent structures in the California current system – sensitivities and limitations. *Geophys. Astrophys. Fluid Dyn.* 2010;1–20.
- [27] Eldredge JD, Chong K. Fluid transport and coherent structures of translating and flapping wings. *Chaos* 2010;20:017509.
- [28] Grover P. Finding and exploiting structure in complex systems via geometric and statistical methods. PhD thesis, Virginia Polytechnic Institute and State University; 2010.
- [29] Stremmler MA, Ross SD, Grover P, Kumar P. Topological chaos and periodic braiding of almost-cyclic sets. *Phys. Rev. Lett.* 2011;106:114101.
- [30] Grover P, Ross SD, Stremmler MA, Kumar P. Topological chaos, braiding and bifurcation of almost-cyclic sets. *Chaos Int J Nonlinear Sci*, in press.
- [31] Kelley Douglas H, Ouellette Nicholas T. Separating stretching from folding in fluid mixing. *Nat. Phys.* 2011. <http://dx.doi.org/10.1038/nphys1941>.
- [32] Mendoza C, Mancho AM. Hidden geometry of ocean flows. *Phys. Rev. Lett.* 2010;105:038501.
- [33] Lasota A, Mackey MC. Chaos, fractals and noise. Stochastic aspects of dynamics. Springer-Verlag; 1994.
- [34] Froyland G. Statistically optimal almost-invariant sets. *Physica D* 2005;200:205–19.
- [35] Dellnitz M, Junge O. Set oriented numerical methods for dynamical systems. Handbook of dynamical systems, vol. 2. Amsterdam: North-Holland; 2002.

- [36] Pesin Y, Barreira L. *Encyclopedia of Mathematics and its applications* 115. Non uniform hyperbolicity. Cambridge University Press; 2007.
- [37] Haller G, Yuan G. Lagrangian coherent structures and mixing in two-dimensional turbulence. *Physica D* 2000;147:352–70.
- [38] Haller G. Distinguished material surfaces and coherent structures in 3D fluid flows. *Physica D* 2001;149:248–77.
- [39] Eeberly D. *Ridges in image and data analysis*. 2nd ed. Kluwer Academic Publishers; 1996.
- [40] Senatore C, Ross SD. Detection and characterization of transport barriers in complex flows via ridge extraction of the finite time Lyapunov exponent field. *Int J Numer Methods Eng* 2011;86:1163–74.
- [41] Winkler S. *Lagrangian dynamics in geophysical fluid flows*. PhD thesis, Brown University; 2001.
- [42] Froyland G, Padberg K. Almost-invariant sets and invariant manifolds connecting probabilistic and geometric descriptions of coherent structures in flows. *Physica D* 2009;238:1507–23.
- [43] Wolf A, Swift JB, Swinney HL, Vastano JA. Determining Lyapunov exponents from a time series. *Physica D* 1985;16:285–317.
- [44] Chen J. *Topological chaos and mixing in lid-drive cavities and rectangular channels*. PhD thesis, Virginia Polytechnic Institute and State University; 2008.
- [45] Dellnitz M, Froyland G, Horenkamp C, Padberg-Gehle K, Gupta AS. Seasonal variability of the subpolar gyres in the Southern Ocean: a numerical investigation based on transfer operators. *Nonlinear Process. Geophys.* 2009;16:655–64.
- [46] Fritzsche D, Mehrmann V. An SVD approach to identifying metastable sets of Markov chains. Technical report from Institut für Mathematik: Technische Universität Berlin; 2006.
- [47] Froyland G, Santitissadeekorn N, Monahan A. Optimally coherent sets in geophysical flows: a new approach to delimiting the stratospheric polar vortex. *Phys. Rev. E* 2010;82:056311.
- [48] Schmale DG, Ross SD, Fetters TL, Tallapragada P, Wood-Jones AK, Dingus B. Isolates of *Fusarium graminearum* collected 40 to 320 m above ground level cause *Fusarium* head blight in wheat and produce trichothecene mycotoxins. *Aerobiologia* 2011. <http://dx.doi.org/10.1007/s10453-011-9206-2>.